

Magmatic and structural controls on porphyry-style Cu–Au–Mo mineralization at Kemess South, Toadoggone District of British Columbia, Canada

Paul Duuring · Stephen M. Rowins ·
Bradley S. M. McKinley · Jenni M. Dickinson ·
Larry J. Diakow · Young-Seog Kim · Robert A. Creaser

Received: 24 March 2008 / Accepted: 1 December 2008
© Springer-Verlag 2009

Abstract Kemess South is the only Cu–Au–Mo mine in the Toadoggone district and a major Cu and Au producer in British Columbia. Porphyry-style Cu–Au–Mo mineralization is mainly hosted by the tabular, SW-plunging, 199.6±0.6-Ma Maple Leaf granodiorite, which intrudes tightly folded, SW-dipping, Permian Asitka Group siltstone and limestone and homogeneous Triassic Takla Group basalt. Southwest-dipping 194.0±0.4-Ma Toadoggone Formation conglomerate, volcanoclastic, and epiclastic rocks overlie the granodiorite and Asitka Group rocks. Minor Cu–Au–Mo mineralization is

hosted by the immediate Takla Group basalt country rock, whereas low-tonnage high-grade Cu zones occur beneath a 30-m-thick leached capping in supergene-altered granodiorite and in exotic positions in overlying Toadoggone Formation conglomerate. Granodiorite has an intrusive contact with mineralized and altered Takla Group basalt but displays a sheared contact with unmineralized and less altered Asitka Group siltstone. The North Block fault is a deposit-scale, E-striking, steeply S-dipping normal fault that juxtaposes the granodiorite/basalt ore body against unmineralized Asitka Group rocks. Younger NW- and NE-striking normal–dextral faults cut all rock types, orebodies, and the North Block fault with displacements of up to 100 m and result in the graben-and-horst-style block faulting of the stratigraphy and ore body. Both basalt and granodiorite host comparable vein sequence and alteration histories, with minor variations in hydrothermal mineral assemblages caused by differing protolith chemistry. Early potassic alteration (and associated early-stage Cu ± Au ± Mo mineralization) is partly replaced by phyllic and intermediate argillic alteration associated with main-stage Cu–Au–Mo mineralization. Two main-stage veins have Re–Os molybdenite ages of 201.3±1.2 and 201.1±1.2 Ma. These mineralization ages overlap the 199.6±0.6-Ma U–Pb zircon crystallization age for the Maple Leaf granodiorite. Late-stage pyrite-rich stringer veins and related phyllic alteration assemblages are cut by anhydrite-rich, carbonate-rich, and chlorite veins. Fluids and metals associated with early-, main-, and late-stage veins were probably derived principally from the same deep magma chamber as the Maple Leaf granodiorite. These magmatic-derived fluids interacted with Asitka and Takla Group country rocks and possibly with meteoric and metamorphic fluids prior to mineralization.

Editorial handling: T. Bissig

P. Duuring (✉) · S. M. Rowins · B. S. M. McKinley ·
J. M. Dickinson
Department of Earth and Ocean Sciences,
University of British Columbia,
Vancouver, British Columbia, Canada V6T 1Z4
e-mail: pduuring@hotmail.com

L. J. Diakow
British Columbia Geological Survey, Ministry of Energy,
Mines and Petroleum Resources,
Victoria, British Columbia, Canada V8V 1X4

Y.-S. Kim
Department of Environmental Geosciences,
Pukyong National University,
Busan, South Korea 608-737

R. A. Creaser
Department of Earth and Atmospheric Sciences,
University of Alberta,
Edmonton, Alberta, Canada T6G 2E3

Present address:

P. Duuring
Department of Environmental Geosciences,
Pukyong National University,
Busan, South Korea 608-737

Keywords Porphyry · gold · copper · Toadoggone · Stikine ·
Kemess South

Introduction

The Toodoggone district is a 100-km-long and 30-km-wide NNW-trending belt of volcano–plutonic rocks located within the Intermontane Belt of the Stikine terrane, about 900 km NNW of Vancouver and 420 km NW of Prince George, in north-central British Columbia. The district contains several significant calc–alkaline porphyry Cu–Au–Mo (e.g., Kemess South, Kemess North, and Pine) and epithermal Au–Ag (e.g., Shasta, Baker, and Lawyers) deposits. Of these porphyry-style deposits, Kemess South is the only operating Cu–Au–Mo mine in the Toodoggone district and a major Cu and Au producer in British Columbia (with a past production to 31 December 2007 of 161 Mt at 0.71 g/t Au and 0.23% Cu, and it has proven plus probable reserves of 51.8 Mt at 0.47 g/t Au and 0.17% Cu: Skrecky, unpublished report for Northgate Minerals Corp., 2008). Recent detailed mapping and core logging at Kemess South define relationships between rock types, structures, and vein and hydrothermal alteration mineral assemblages. Laboratory-based techniques, including fluid inclusion and stable isotope studies, are used to constrain hydrothermal fluid conditions at the time of mineralization, as well as likely source areas for the fluids and metals. This paper provides a genetic model that describes key magmatic and structural processes that influenced the present geometry of the Kemess South Cu–Au–Mo ore body. The Kemess South deposit model is important in that it provides a basis for the testing of possible genetic links between porphyry Cu–Au ± Mo and epithermal Au ± Ag deposits in the Toodoggone district (Duuring et al. 2008).

Methodology

Detailed lithological and structural mapping was performed in the Kemess South mine at 1:500 and 1:1,000 scales. Access to the base of the north wall was limited due to pit wall instability. Five widely spaced diamond drill holes (i.e., KE-04-02, KS-04-03, KS-04-14, KS-04-04, and 90-02) that define an ENE–WSW long section through the deposit were studied in detail, with emphasis on relationships between lithology, structure, hypogene alteration, and Cu–Au–Mo mineralization. Hand specimens of least-altered rocks were collected from exposures in the pit and diamond drill core for petrographic analysis. Structural orientations are given as dip angle/dip direction or plunge/trend orientations, with reference to True North, unless otherwise indicated; where strikes are indicated, right-hand rule is observed. The present-day surface at Kemess South is labeled the 1,300-m elevation level (i.e., the 1,300 mRL). At the time of mapping, the pit floor is

at 1,200±30 mRL. The base of supergene weathering varies from about 50 m below the present surface in the NE of the pit to a depth of at least 268 m in the SW. Hand specimens of least-altered rocks and hypogene alteration assemblages to veins were etched by hydrofluoric acid and stained by sodium cobaltinitrite to aid in the identification of feldspars and mineral proportion estimation (i.e., point counting).

Pyrite, chalcopyrite, and anhydrite were handpicked from crushed unweathered vein samples for sulfur isotope studies. Sulfur isotope analyses were undertaken at the G.G. Hatch Isotope Laboratories, University of Ottawa, Canada. Samples were weighed into tin capsules with tungsten oxide (WO₃) and loaded into a VarioEL III elemental analyzer to be flash-combusted at 1,800°C in the presence of oxygen. Released gases were carried by ultra-pure helium through the instrument to be cleaned and separated. The SO₂ gas was then carried into the DeltaPlus isotope ratio mass spectrometer (ThermoFinnigan, Germany) for analysis. Calcite was handpicked from crushed vein samples and submitted for carbon and oxygen stable isotope analysis at the G.G. Hatch Isotope Laboratories, University of Ottawa, Canada. The δ¹³C and δ¹⁸O values were determined using a Delta XP and a Gas Bench II following the methods of Coplen et al. (1983) and Al-Asam et al. (1990).

Re–Os dating of molybdenite hosted by quartz-rich vein hand specimens was conducted at the Radiogenic Isotope Facility, University of Alberta. Detailed description of the methods used for the extraction and analysis of molybdenite is described by Selby and Creaser (2004), modified with the use of a mixed double spike (Markey et al. 2007). The samples were processed by metal-free milling and grinding, followed by density and magnetic separation to produce a molybdenite concentrate. The ¹⁸⁷Re and ¹⁸⁷Os concentrations in molybdenite were determined by isotope dilution mass spectrometry using Carius tube, solvent extraction, anion chromatography, and negative thermal ionization mass spectrometry techniques. A mixed double spike containing known amounts of isotopically enriched ¹⁸⁵Re, ¹⁹⁰Os, and ¹⁸⁸Os was used. Isotopic analysis was done using a Micromass Sector 54 mass spectrometer with a Faraday collector. Total procedural blanks for Re and Os were less than 3 and 1 pg (<20 fg ¹⁸⁷Os), respectively. These procedural blanks are insignificant in comparison to the Re and Os concentrations in molybdenite. The Chinese molybdenite powder HLP-5 (Markey et al. 1998), which is used as an in-house control sample by AIRIE, Colorado State University, is also routinely analyzed at the University of Alberta. For this control sample, a Re–Os date of 220.0±1.0 Ma was determined at the time of the Kemess South molybdenite analysis. This age is identical to that reported by Markey et al. (1998).

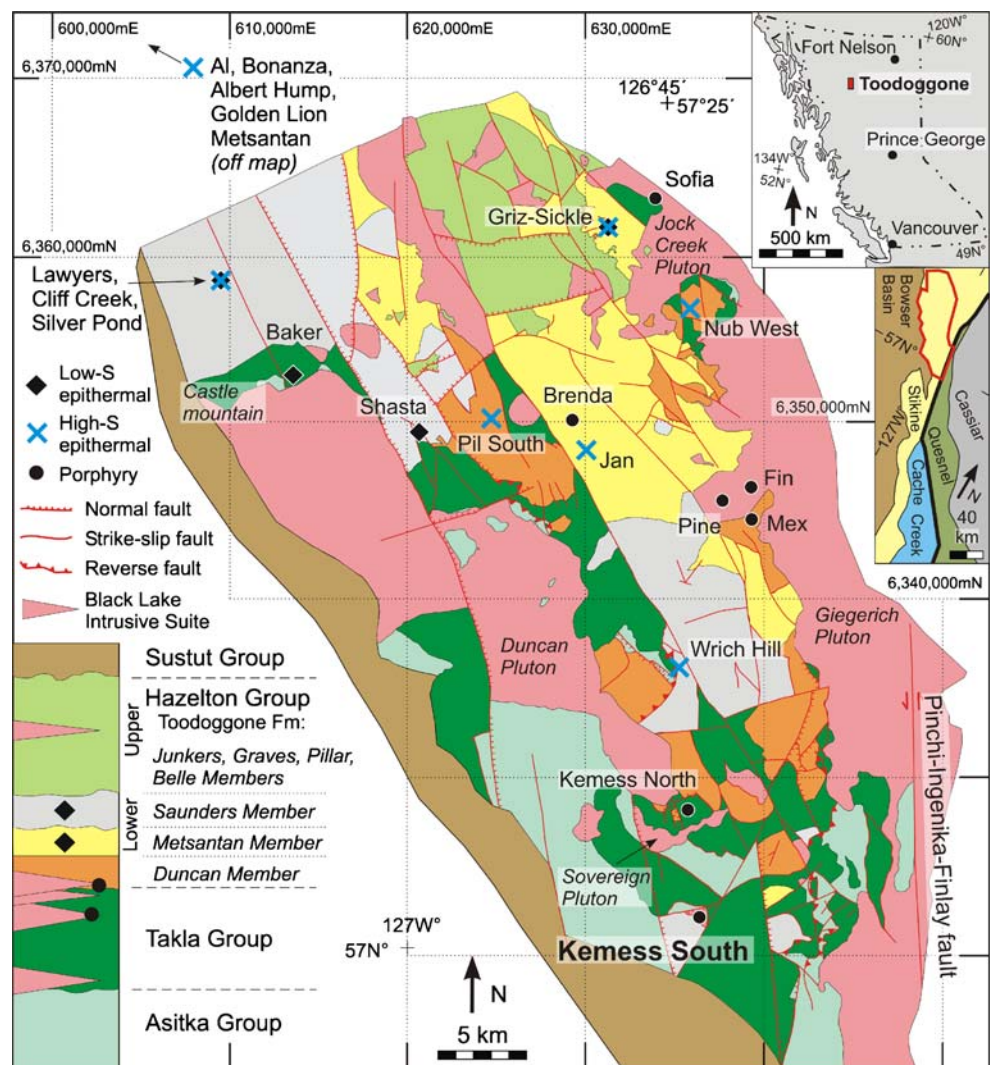
Regional geology

The Canadian Cordillera comprises a succession of allochthonous volcanic arcs and accretionary complexes that resulted from the subduction of the Panthalassa oceanic plate and the Pacific ocean basins beneath the continental and oceanic North American plate (Monger and Nokleberg 1996). The NNW-trending Toodoggone district occurs within the Mesozoic Intermontane Belt and comprises island-arc volcano-plutonic rocks located near the ENE margin of the Stikine terrane. The Stikine terrane formed outboard from ancestral North America and is currently juxtaposed against Quesnel terrane rocks by the sinistral Pinchi-Ingenika-Finlay fault (Fig. 1). The Jurassic–Cretaceous Bowser Basin overlaps the Stikine terrane to the west of the Toodoggone district (Fig. 1).

The oldest known basement rocks in the Toodoggone district are submarine island-arc rhyolitic and basaltic volcanic rocks, siltstone, and limestone of the Lower Permian Asitka Group (ca. 308 Ma, Diakow 2001). These

rocks are unconformably overlain by basaltic lava, with interbedded lapilli tuff and volcanic breccia units of the Middle Triassic Takla Group (ca. 216 Ma; Monger and Church 1977). Asitka and Takla Group rocks are chiefly fault-bound and exposed in the southern half of the Toodoggone district, adjacent to exposed plutons (Fig. 1). Locally, Asitka Group rocks form roof pendants to plutons. The basement rocks are unconformably overlain by Upper Triassic to Lower Jurassic Hazelton Group volcanic and sedimentary rocks (Diakow et al. 1991, 1993). Hazelton Group rocks are exposed throughout the Stikine terrane and are locally represented in the Toodoggone district by the Lower Jurassic (ca. 201 to 188 Ma; Diakow 2001, 2006a; Diakow et al. 1991; Dickinson 2006) Toodoggone Formation, which is at least 2.2 km thick and divided into two subaerial eruptive sequences that were deposited during two discrete volcanic cycles (Diakow et al. 1993). The lower sequence includes the Duncan, Metsantan, and Saunders Members, which comprise dacitic ash-flow tuffs and high-silica andesite lava flows. The upper sequence is defined by

Fig. 1 The simplified geology map of the southern half of the Toodoggone district, south of the Toodoggone river, shows the distribution of rock types, structures, and porphyry Cu–Au–Mo and epithermal Au ± Ag occurrences. The geological interpretation is based on regional mapping reported by Diakow (2001; 2004; 2006a) and Diakow et al. (2005). The two inset maps show the location of the Toodoggone district in British Columbia and the relationship between the district and recognized terranes in British Columbia (the outline of the southern Toodoggone district is defined by a thick red line, whereas the Pinchi-Ingenika-Finlay fault that separates the Stikine and Quesnel terranes is delineated by a thick black line)



the Junkers, Graves, Pillar, and Belle Members and contains dacitic tuffs that are similar to those of the lower sequence but also includes basalt–basaltic andesite flows, rhyolite, and minor volcanic-derived sedimentary rocks (Diakow 2006a, b; Diakow et al. 1991, 1993). At least 80 km² of Toodoggone Formation rocks are exposed throughout the district within a NW-trending volcanic–sedimentary depression (Diakow et al. 1993). Most Toodoggone Formation rocks are concentrated in the northern half of the district, with only the lower members of the Toodoggone Formation exposed with Asitka and Takla Group basement rocks in southernmost areas (Fig. 1). Lower to Upper Cretaceous continental clastic rocks of the Sustut Group overlap the western margin of the Toodoggone district (Fig. 1) but only minor remnants of near-horizontally bedded Sustut Group rocks cap Toodoggone Formation rocks within the district. Toodoggone Formation rocks have undergone up to zeolite-facies regional metamorphism, with underlying Takla Group rocks having experienced prehnite–pumpellyite metamorphism (Diakow et al. 1993). These metamorphic mineral assemblages are interpreted to be caused by burial metamorphic conditions (Diakow et al. 1993). High-temperature contact metamorphism is locally associated with plutonic rocks and dikes. Consequently, the prefix “meta” is implied but omitted from lithological descriptions that follow.

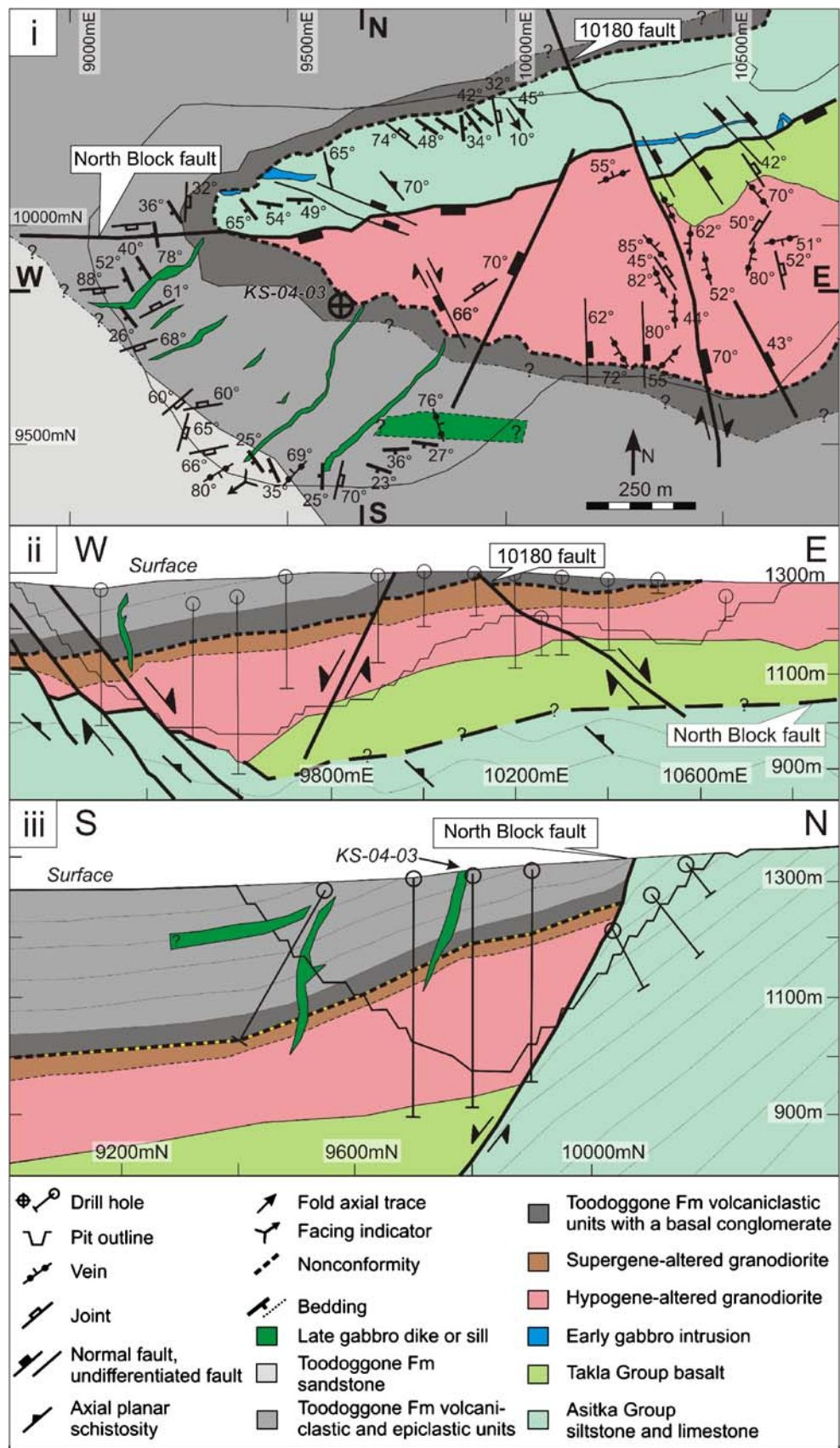
Asitka, Takla, and Hazelton Group volcano–sedimentary rocks are intruded by Upper Triassic to Lower Jurassic felsic to intermediate plutons and cogenetic dikes of the Black Lake suite (Diakow 2001, 2006b; Diakow et al. 1993; Mortensen et al. 1995). The plutons are exposed along the margins of the Toodoggone volcanic–sedimentary depression but also occur internally within the depression as elongate NW- to NE-trending plutons (Fig. 1). Plutonism occurred episodically from ca. 218 to 191 Ma (Diakow 2006b; Dickinson 2006; Mortensen et al. 1995), with most dated plutons appearing to have intruded after tectonic uplift and erosion at ca. 202 to 197 Ma (Diakow et al. 1993). Plutons are commonly cut by several generations of NNE- to NW-trending dikes of compositions ranging from rhyolite to basalt, with andesite being most common (Diakow et al. 1993). Felsic dikes cut their respective plutonic rocks and Duncan Member Toodoggone Formation rocks at the Kemess North (McKinley 2006) and Pine (Dickinson 2006) porphyry deposits. These temporal relationships suggest that felsic intrusive magmatism is broadly coeval with Toodoggone Formation volcanism.

Porphyry Cu–Au ± Mo mineralization is the earliest mineralization event in the district, occurring between ca. 221 Ma (Re–Os on molybdenite age for Mo mineralization at Fin; Dickinson 2006) and ca. 194 Ma (U–Pb on zircon age for a weakly mineralized syenite dike at Pine; Dickinson 2006) and with mineralization most abundant

between ca. 202 and 197 Ma (Diakow 2006b; McKinley 2006; Mortensen et al. 1995). High-sulfidation epithermal systems (e.g., Silver Pond, Griz-Sickle, Al, Pil South, Nub West) are hosted by Toodoggone Formation rocks and range in age from 201 to 188 Ma (Clark and Williams-Jones 1991; Diakow et al. 1991), thereby overlapping the 202 to 197 Ma porphyry event and the earliest stages of Toodoggone Formation volcanism and suggesting a possible genetic link between plutonism, porphyry mineralization, volcanism, and high-sulfidation epithermal mineralization. Low-sulfidation epithermal Au–Ag and Ag–Au occurrences (e.g., Shasta, Baker, Lawyers, Griz-Sickle, Wrich Hill) are hosted by Takla Group and Toodoggone Formation rocks and range in age from ca. 192 to 162 Ma (Clark and Williams-Jones 1991; Diakow et al. 1991), which coincides with the last phases of felsic dike emplacement, volcanism, and fault-block subsidence at ca. 186 Ma.

Bedding contacts define rare outcrop-scale, recumbent, and inclined plunging folds in Asitka and Takla Group rocks, whereas bedding in Sustut Group rocks locally defines large-scale east-verging folds (Diakow et al. 1993). The volcano–sedimentary rocks in the Toodoggone district are bounded and cut by kilometer-scale, NNW-trending, steep-dipping faults that probably represent major intra-arc extensional structures that formed within a broader magmatic arc (Diakow et al. 1993). Displacement and movement sense indicators are rarely observed in the Toodoggone district. Where they are reported, most faults display normal displacement, with rare strike-slip movements (Diakow et al. 1991). In all areas of the Toodoggone district, NW-trending faults are locally cross-cut by NE-trending steep-dipping faults. East–west-trending faults cut all stratigraphic groups and their timing with respect to NW-trending faults is variable (Diakow et al. 1993). Northwest-trending faults control the emplacement of plutons and dikes and have influenced the formation of porphyry and epithermal mineralization (Diakow et al. 1991, 1993). Northwest- to NE-trending steep-dipping faults displace Asitka Group, Takla Group, and Toodoggone Formation rocks with dominantly normal displacement to produce horst-and-graben geometries, with the Toodoggone Formation rocks situated in down-dropped grabens that are bound by NW-trending normal faults (Fig. 1). Strike-slip faults along the eastern margin of the Toodoggone volcanic depression demonstrate dextral displacement of about 5 km and are interpreted to have formed during the Late Cretaceous or younger (Diakow et al. 1991). The rare occurrence of NW- to NE-trending thrust faults that displace Asitka Group rocks on top of Toodoggone Formation rocks (Fig. 1) are possibly the result of broad regional E–W shortening during either the mid-Jurassic or Cretaceous (Diakow et al. 1991).

Fig. 2 Geological map and sections for Kemess South: (i) the simplified geological plan shows the distribution of major rock types and structures. Note the position of the north–south cross section line (N–S), the east–west long-section line (W–E), and the logged diamond drill hole, KS-04-03 (Fig. 4). The granodiorite demonstrates a sharp tectonic contact with Permian Asitka Group siltstone but an irregular intrusive contact with Triassic Takla Group rocks. These rocks are unconformably overlain by Toodoggone Formation conglomerate, volcanoclastic, and epiclastic rocks. (ii) The west–east long section through the mine stratigraphy demonstrates the truncation of the moderately SW-plunging tabular granodiorite and Takla Group basalt by the North Block fault. The mine stratigraphy and E–W striking North Block fault are displaced by NE- to NW-trending normal faults (e.g., the 10180 fault). (iii) The simplified south–north cross section demonstrates the truncation of the shallowly dipping granodiorite and overlying Toodoggone Formation rocks by the North Block fault



Kemess South geology

Rock types

Asitka Group siltstone and limestone

Well-bedded Permian Asitka Group siltstone crops out in the north wall of the pit (Fig. 2 i). The west, north, and eastern limits of the Asitka Group rocks were not defined during pit mapping as they occur under cover outside the pit extent. Least-altered siltstone is gray-green and com-

prises fine-grained massive quartz (95 vol.%), with minor chlorite (5%). Locally, siltstone is interbedded with gray limestone that contains solitary coral fossils. Planar beds in the siltstone are 10 to 15 cm thick and regularly spaced (Fig. 3 i). Bedding orientations vary due to their recumbent folding but they are mostly SE striking and dip 40° to 65° to the SW. Bedding in the siltstone steepens with proximity to and is truncated by the North Block fault. Asitka Group units are cut by minor quartz-calcite-pyrite veins but do not host intense hypogene alteration or anomalous Au, Cu, or Mo grades.

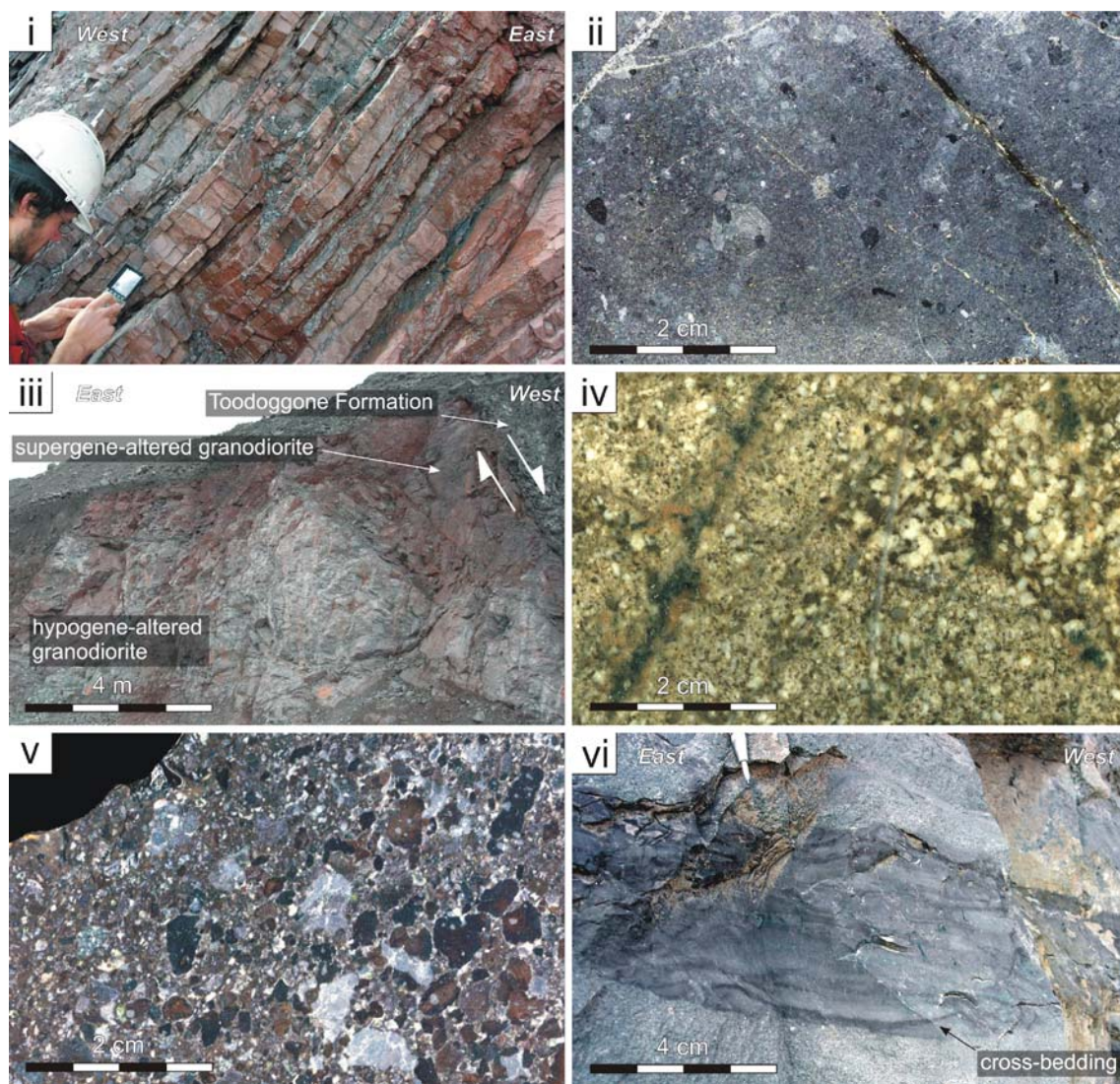


Fig. 3 Photographs of representative rock types at Kemess South: (i) Asitka Group siltstone near the present surface in the north wall of the pit displays regularly spaced planar beds. (ii) Massive porphyritic Takla Group basalt contains hexagonal, partly chloritized, hornblende phenocrysts in a groundmass of chlorite, plagioclase, biotite, and hornblende. (iii) The south wall of the pit displays hypogene-altered granodiorite overlain by supergene-altered granodiorite and a sharp faulted contact with overlying Toodoggone Formation volcaniclastic

rocks. (iv) Granodiorite is massive, coarse-grained, and porphyritic with phenocrysts of plagioclase, alkali feldspar, biotite, and hornblende. (v) The hand specimen of a Toodoggone Formation volcaniclastic rock is supergene-altered (hematite rich), coarse-grained, poorly sorted, lithic fragment rich, and andesitic in composition. (vi) The Toodoggone Formation in the south wall of the pit displays an 80-cm-thick cross-bedded siltstone unit bordered by coarser-grained well-sorted sandstone

Takla Group basalt

Least-altered Triassic Takla Group basalt crops out as a wedge-shaped body to the north of the granodiorite (Fig. 2 i) and is intersected by drill holes beneath the pluton (e.g., diamond drill hole KS-04-03, Figs. 2 ii and 4). Although the contact with the granodiorite is locally strained, the irregular morphology of the contact suggests that this is an intrusive contact. The north margin of the basalt is defined by the North Block fault, which juxtaposes the basalt with Asitka Group siltstone. Least-altered basalt is green and massive but is locally porphyritic, with 1- to 5-mm-diameter phenocrysts of hexagonal hornblende (5%) and

bladed plagioclase (5%) surrounded by a groundmass of chlorite (40%), plagioclase (30%), hornblende (10%), and epidote (10%; Fig. 3 ii). Hydrothermal chlorite partly pseudomorphs hornblende, whereas epidote replaces plagioclase. No primary compositional layering, bedding, or other facing directions are preserved in the basalt.

Maple Leaf granodiorite

Gold–Cu–Mo mineralization at Keness South is predominantly hosted by the moderately (40°) SW-plunging 199.6± 0.6-Ma (Mortensen et al. 1995) Maple Leaf granodiorite pluton. The granodiorite crops out in the center of the pit

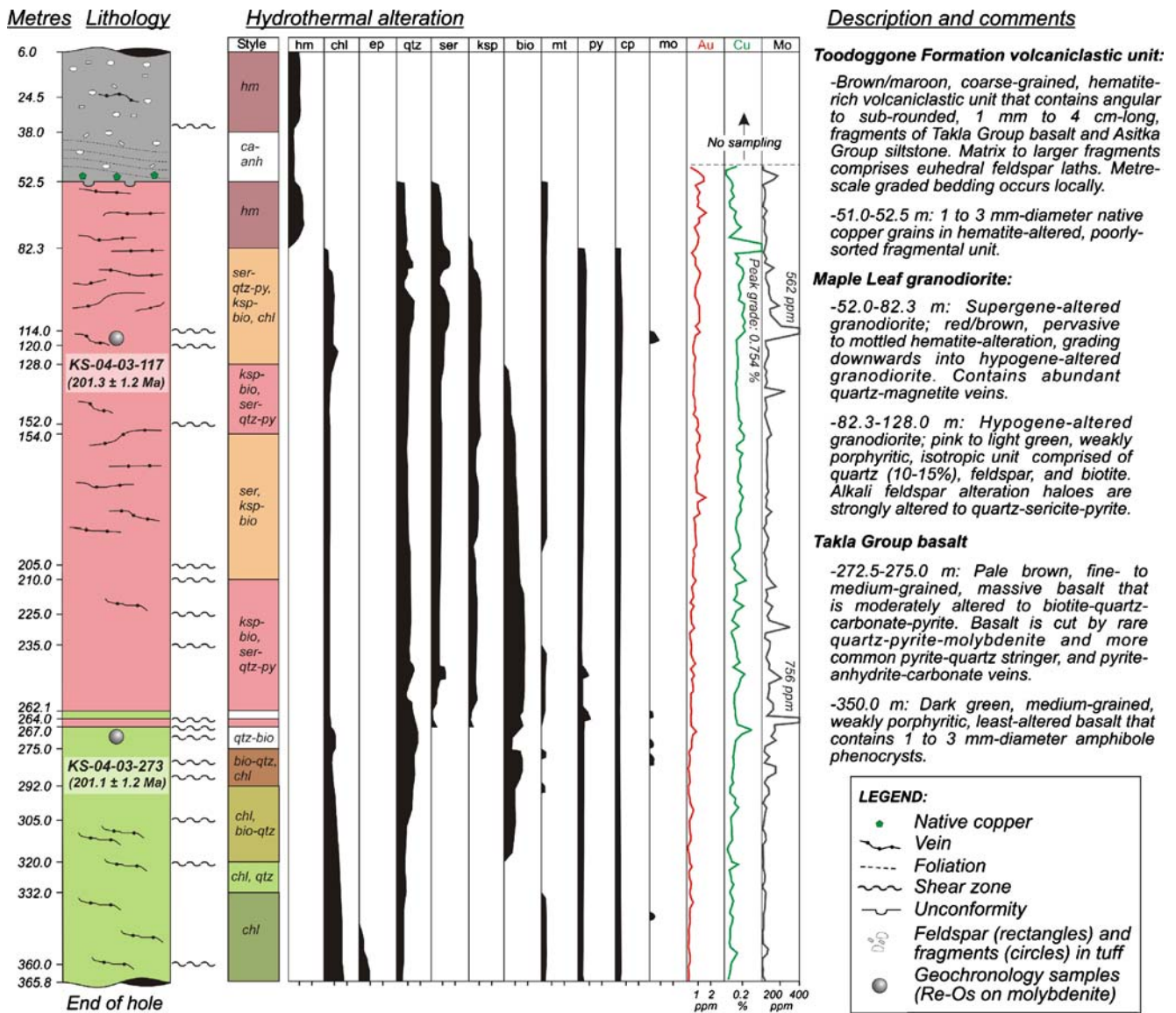


Fig. 4 Diamond drill hole KS-04-03 was drilled from surface at an inclination of -90° from a collar located at 9,697 m E, 9,749 m N (mine grid) and an elevation of 1,217 m. The Maple Leaf granodiorite has an upper nonconformable contact with Toodoggone Formation conglomerate and a lower intrusive contact with

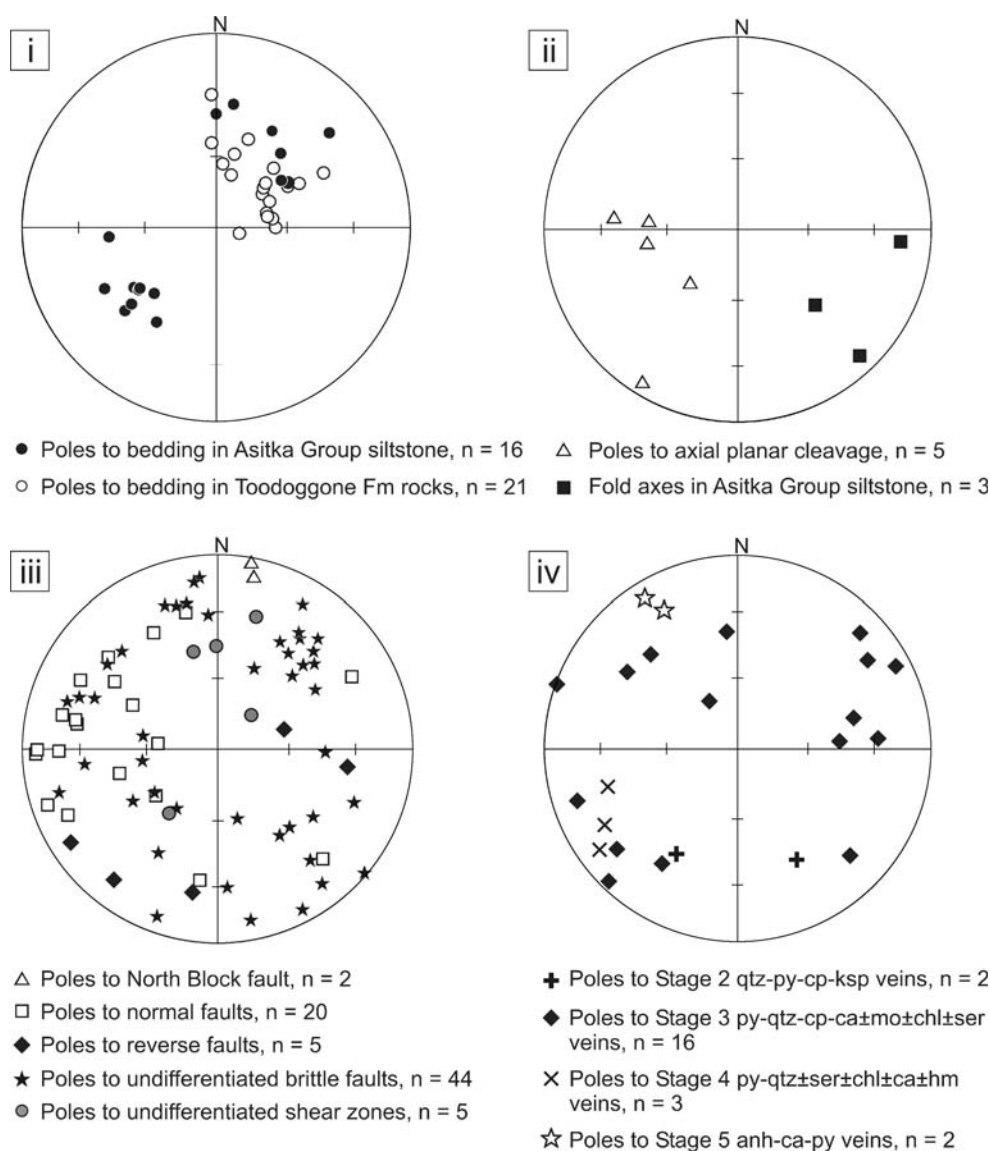
Takla Group basalt. Hydrothermal alteration minerals and metals occur in both rock types either side of the intrusive contact. Abbreviations: anh, anhydrite; bio, biotite; ca, calcite; chl, chlorite; cp, chalcopyrite; ep, epidote; hm, hematite; ksp, alkali feldspar; mo, molybdenite; mt, magnetite; py, pyrite; qtz, quartz; ser, sericite

(Fig. 2 i) and displays a tectonic contact with Asitka Group siltstone, an intrusive relationship with Takla Group basalt, and an unconformable and locally tectonic contact with overlying Toodoggone Formation rocks (Fig. 3 iii). The original morphology of the granodiorite pluton at the time of its emplacement is difficult to determine owing to the presently eroded upper contact of the granodiorite and the fault-truncated northern margin (Fig. 2 i). Unaltered granodiorite is not exposed in the Kemess South pit due to pervasive replacement associated with several successive hydrothermal alteration events. Where present, least-altered granodiorite is pale brown to cream, massive, coarse-grained, and porphyritic to equigranular. Primary igneous minerals include plagioclase (35%), alkali feldspar (25%), quartz (20%), biotite (10%), and hornblende (5%); hydrothermal biotite, alkali feldspar, chlorite, sericite, and pyrite constitute up to 5 vol.% of the least-altered rock (Fig. 3 iv).

Toodoggone Formation rocks

The 194.0 ± 0.4 -Ma (Diakow 2001) Saunders Member Toodoggone Formation unconformably overlies supergene-altered Asitka Group siltstone and granodiorite (Figs. 2 iii and 4). The formation comprises a 5- to 15-m-thick basal polymictic conglomerate that is overlain by a 150- to 200-m-thick sequence of interbedded volcanic and volcanoclastic andesite (Fig. 3 v) and an upper >20-m-thick sequence of epiclastic sandstone and siltstone (Fig. 3 vi). Bedding in the Toodoggone Formation strikes E-W to NW-SE and dips shallowly to moderately (20° to 40°) to the SW (Fig. 2 i). The basal conglomerate is brown/maroon, coarse-grained, poorly sorted, and hematite rich and contains angular to subrounded 5-mm- to 1-m-diameter clasts of Takla Group basalt, Asitka Group siltstone, and porphyritic to equigranular felsic igneous rocks. The matrix includes

Fig. 5 Lower-hemisphere equal-area stereoplots of selected planar and linear structural elements: (i) Sedimentary beds in Asitka Group siltstone and Toodoggone Formation units. (ii) Fold axes and axial planar cleavage to isoclinal folds in Asitka Group siltstone. (iii) Fault and shear zones cutting all rock types. (iv) Vein types in granodiorite (note that stage 3 veins are associated with main-stage Cu–Au–Mo mineralization)



fragments of euhedral plagioclase laths, quartz, hornblende, and biotite. Native copper and malachite (1- to 20-mm diameter) occur locally in the basal conglomerate within 10 m of the unconformable contact with granodiorite and Asitka Group siltstone. Meter-scale graded-bedding occurs locally and indicates that the sequence youngs from base to top. The basal conglomerate is conformably overlain by a sequence of interlayered andesitic tuffs and crystalline andesitic lavas and/or sills. Mineral proportions vary widely in these rocks; however, most rocks contain plagioclase (15% to 40%), hornblende (10% to 20%), biotite (10% to 20%), chlorite (10% to 30%), quartz (10%), hematite (10%), and epidote (5%). The volcanoclastic rocks commonly include angular clasts of reworked crystalline andesite (10% to 40%). Individual planar beds are 1 to 10 m thick and graded bedding occurs locally. A 10- to 20-m-thick basalt unit occurs near the transition between volcanoclastic and epiclastic units in the south wall of the pit (Fig. 2 i). It is uncertain if this basalt unit is a sill or a flow because it is massive and homogeneous and lies parallel to bedding in the Toodoggone Formation. Epiclastic units, such as sandstone and siltstone, crop out in the SW wall of the pit and are the youngest Toodoggone Formation rocks presently exposed in the pit. Siltstone and sandstone comprise quartz (40%), plagioclase (30%), chlorite (15%), and hematite (15%). The units are well sorted and fine- to coarse-grained and locally display graded and cross-bedding (Fig. 3 vi).

Gabbro dikes

Two generations of gabbro intrusions occur at Kemess South. The earlier gabbro intrudes Asitka Group siltstone in the NW and NE walls of the pit (Fig. 2 i). The dikes are 1 to 15 m thick and E-striking and dip steeply (70° to 80°) to the south. The gabbro cuts Asitka Group siltstone subparallel to bedding but locally bifurcates to form 1-m-thick dikes that intrude along a strongly developed, NW-striking, and NE-dipping schistose fabric in the siltstone. This first generation of gabbro is truncated by the Toodoggone Formation basal nonconformity and thus intruded before deposition of these units (i.e., before 194.0 ± 0.4 Ma).

A second generation of gabbro dikes cut bedding in Toodoggone Formation rocks in the SW of the pit (Fig. 2 i). The dikes are 5 to 30 m thick, NE-trending, and subvertical. The distribution of the dikes is well-constrained by pit wall mapping and through intersections in the pit floor during routine grade control drilling. The dikes are thickest in the Toodoggone Formation units but narrow with proximity to the granodiorite contact and are rarely observed in the granodiorite (Fig. 2 i). Second-generation dikes are indistinguishable in terms of their texture and mineralogy from first-generation gabbro intrusions.

Structure

Sedimentary beds in Asitka Group siltstone trend NW and dip moderately (30° to 60°) to the SW and NE (Fig. 5 i). Locally, the siltstone beds define tight to isoclinal and shallow to steeply (10° to 80°) SE-plunging folds that have an axial planar cleavage (S_1) that strikes N to NW and dips mainly 30° to 60° to the E to NE (Figs. 5 b and Fig. 6 i). First-generation gabbro dikes intrude along bedding and S_1 axial planar cleavage planes in siltstone (Fig. 6 ii). Isoclinal folds in Asitka Group siltstone are cut by NW-striking and NE-dipping (i.e., axial planar parallel) reverse faults (Fig. 6 iii). Bedding either side of the reverse fault commonly displays centimeter-scale drag fold relationships. The bedding, isoclinal folds, axial planar cleavage, and reverse faults are truncated by the Toodoggone Formation basal nonconformity and are overlain by shallowly (20°) SW-dipping conglomerate and volcanoclastic units (Fig. 6 iii). Beds in Toodoggone Formation rocks are SE striking and dip shallowly to moderately (10° to 70°) to the SW (Fig. 5 i). Unlike Asitka Group rocks, beds in the Toodoggone Formation do not show macro-folds or the S_1 fabric. Interestingly, the early structural relationships in the Asitka Group siltstone at Kemess South are similar to early structures documented elsewhere in the Toodoggone district; for example, recumbent folds with subhorizontal axial planes occur in Asitka Group chert at Castle Mountain (Fig. 1). At this location, fold hinges are also locally offset by axial planar-parallel shear zones (Diakow et al. 1993). These structures suggest that SW–NE shortening coincided with tight folding and reverse faulting prior to the uplift, erosion, and deposition of Toodoggone Formation units at ca. 194 Ma at Kemess South and elsewhere in the Toodoggone district.

The E-striking and steeply S-dipping “North Block fault” is a deposit-scale fault or shear zone that cuts all lithologies in the pit (Figs. 2 i and 6 iv). The North Block fault is 1 to 5 m wide, infilled by graphite, and juxtaposes unmineralized Asitka Group siltstone against Cu–Au–Mo-mineralized granodiorite in the center of the pit (Fig. 6 v). In the west wall of the pit, the fault juxtaposes shallow-dipping Toodoggone Formation units against more steep-dipping Asitka Group siltstone (Fig. 2 iii). Strain increases in all lithologies within 50 m of the North Block fault, where it is exemplified by subparallel subsidiary faults and related fractures. Locally, S and C shear fabrics within the North Block fault indicate that the last preserved movement sense was normal, S-side-down (Fig. 6 iv). The timing and magnitude of displacement on the fault are interpreted from the abrupt termination of the >300-m-thick granodiorite against the North Block fault and its absence in the siltstone directly to the north of the fault (Fig. 2 ii). These relationships suggest that several hundreds of meters of

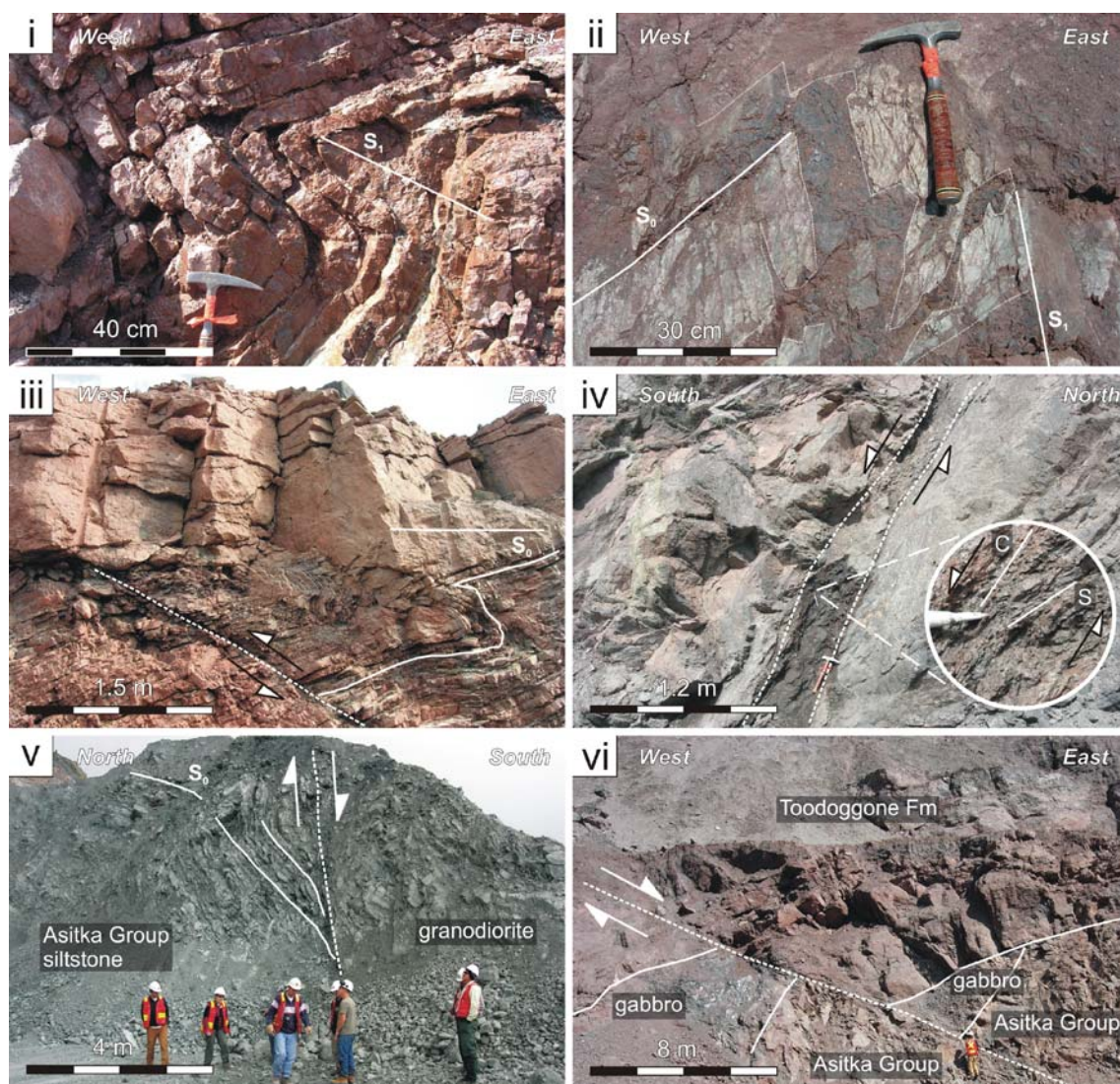


Fig. 6 Pit photographs of structural relationships at Kemess South: (i) Asitka Group siltstone in the north wall displays tight to isoclinal SE-plunging folds that have an axial planar cleavage (S_1) that strikes N to NW and mainly dips 30° to 60° to the E to NE. (ii) A first-generation gabbro dike intrudes along bedding (S_0) and the well-developed axial planar schistosity (S_1) in Asitka Group siltstone in the north wall. (iii) Tight to isoclinally folded beds in Asitka Group siltstone are cut by a NW-striking and NE-dipping reverse fault in the north wall. Both structures are truncated by the Toodoggone Formation basal nonconformity and are overlain by shallowly (20°) SW-dipping conglomerate and volcanoclastic units. (iv) The E-striking and steeply S-dipping normal North Block shear zone cuts Toodoggone Formation volcani-

clastic rocks in the west wall of the pit. The *inset photograph* shows a close-up of S and C shear plane relationships that indicate that the last phase of movement along the shear zone was normal and S-side-down. (v) An N–S-striking temporary digging face in the center of the pit (10,000 m N; 9,750 m E) demonstrates the faulted contact between Asitka Group siltstone and granodiorite. Siltstone beds steepen towards the North Block fault. Parallel subsidiary faults are more common within 20 m of the contact. (vi) The northwest corner of the pit displays a series of subparallel NW-striking and NE-dipping normal faults. In this example, Asitka Group siltstone, a first-generation gabbro dike, and the unconformably overlying Toodoggone Formation rocks display about 30 m of normal displacement

normal displacement occurred along the fault after the emplacement of the granodiorite (i.e., after ca. 199 Ma) but before deposition of Toodoggone Formation rocks at ca. 194 Ma. The ~ 80 m normal offset of Toodoggone Formation rocks by the North Block fault in the western area of the pit indicates that the fault was reactivated after uplift of the mine stratigraphy and the deposition of the Toodoggone Formation.

Brittle NW- to NE-trending faults occur throughout the deposit and cut all rock types. The faults are moderate to steep dipping, with mostly SW to SE dips (Figs. 5 iii and 6 vi). Deposit-scale faults, such as the NW-striking and steeply NE-dipping “10180” fault in the center of the pit, offset all rock types, the ore body, and North Block fault with a normal–dextral, E-side-down, displacement of about 50 m (Fig. 2 i and ii). Locally, the normal faults display horse-tail

jog geometries and D and R shear plane relationships that indicate normal–dextral displacement. Northeast-trending and steep-dipping normal faults cut all rock types, the North Block fault, and have a similar relative timing to NW-trending normal faults. A deposit-scale NE-trending fault in the center of the pit displays normal west-side-down displacement that juxtaposes Toodoggone Formation rocks against granodiorite (Fig. 3 iii). North–south shortening occurred after deposition of the ca. 194-Ma Toodoggone Formation rocks and resulted in dextral–normal NW-trending faults and contemporaneous NE-trending normal faults. The common occurrence of NW-trending normal faults in Asitka Group siltstone suggests that they are formed, at least in part, by the reactivation of the existing NW-trending axial planar cleavage and reverse faults. Movement along NW- to NE-trending faults resulted in the horst-and-graben block faulting of the mine stratigraphy and ore body. The best example of this deformation style occurs in the center of the pit where a central block of granodiorite is flanked by down-dropped granodiorite either side of NW- and NE-trending faults (Fig. 2 i).

Vein paragenesis

Kemess South veins are divided into seven stages based on their vein mineralogy, texture, and cross-cutting relationships (Fig. 7). These vein types are grouped into early-, main-, late-, and post-mineralization-stage veins based on the presence and concentration of Au or Cu. The veins are discussed below in order of their relative age.

Early-stage mineralization veins: stage 1 and 2 veins

Stage 1 veins are the earliest vein type, occurring only in granodiorite. Although the modal abundance of minerals

varies between individual veins, stage 1 veins mainly comprise quartz (70%), pyrite (10%), and biotite (10%), with minor alkali feldspar (5%), chalcocopyrite (3%), and magnetite (2%). The veins are commonly 1 to 4 mm thick, have diffuse margins, form microvein networks, and are associated with secondary biotite, which defines early potassic alteration zones (Fig. 8 i).

Stage 2 veins cut stage 1 veins in granodiorite (Fig. 8 i) and occur in Takla Group basalt within 50 m of the granodiorite contact. Stage 2 veins are quartz rich (>80%) and contain lesser quantities of pyrite (5% to 10%), chalcocopyrite (5%), calcite (5%), magnetite (2%), and alkali feldspar (2%), with trace molybdenite and gold. Stage 2 veins are commonly 1 cm thick, have straight vein margins, and have a medial zone defined by pyrite, chalcocopyrite, and calcite. The veins are locally rimmed by up to 1-cm-wide pink alkali feldspar alteration halos in granodiorite that stain yellow when reacted with sodium cobaltinitrite (Fig. 8 ii). In Takla Group basalt, stage 2 veins have the same mineralogy as the granodiorite-hosted stage 2 veins, with the exception that biotite forms instead of alkali feldspar. These stage 2 veins are surrounded by up to 4-cm-wide quartz–biotite–pyrite–chalcocopyrite alteration zones. Stage 2 veins and their associated potassic alteration zones are responsible for early-stage Cu–Au–Mo mineralization.

Main-stage mineralization veins: stage 3 veins

Stage 3 veins cut stage 1 and 2 veins in granodiorite and cut stage 2 veins in basalt. Stage 3 veins are up to 4 cm thick and comprise pyrite (10% to 40%), quartz (30% to 60%), and chalcocopyrite (5% to 10%), with minor sericite (10%), chlorite (5% to 10%), calcite (5%), and molybdenite (1%), and trace bismuthinite, pyrrhotite, apatite, barite, bornite, and tennantite. Vein textures include single-phase extensional veins and multistage antitaxial veins. Extensional veins commonly contain chalcocopyrite–molybdenite–pyrite–calcite, with quartz mineral growth fibers oriented perpendicular to vein margins. Multistage antitaxial veins commonly contain two or more microfractures that are oriented within 20° of vein margins. Pyrite and bornite are rare constituents of multistage veins; where they occur in the same vein, they formed during separate stages of vein opening. The multistage veins have highly variable strikes but most have moderate to steep dips (20° to 90°, Fig. 5 iv). Stage 3 veins commonly have a well-developed 1- to 10-cm-wide alteration halo defined by quartz–chlorite–pyrite in basalt (Fig. 8 iii) or quartz–pyrite ± sericite ± chlorite in granodiorite (Fig. 8 iv). Stage 3 veins and their associated alteration halos characterize the phyllic and/or intermediate argillic alteration events at Kemess South and coincide with the main stage of Cu–Au–Mo mineralization.

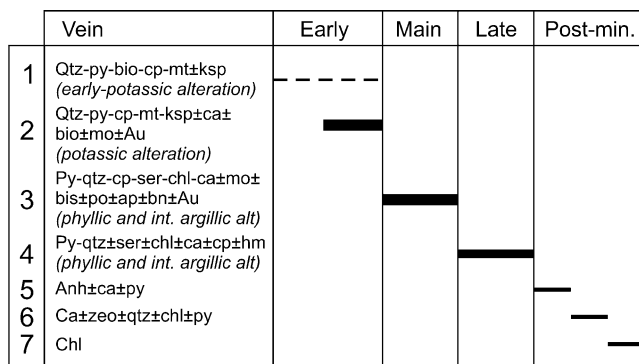


Fig. 7 Veins are divided into early, main, late, and post-mineralization stages. Line thicknesses represent the relative abundance of these veins at Kemess South. Abbreviations: alt, alteration; ap, apatite; anh, anhydrite; bio, biotite; bn, bornite; ca, calcite; chl, chlorite; cp, chalcocopyrite; ep, epidote; hm, hematite; int, intermediate; ksp, alkali feldspar; mo, molybdenite; mt, magnetite; pc, plagioclase; po, pyrrhotite; py, pyrite; qtz, quartz; ser, sericite; zeo, zeolite

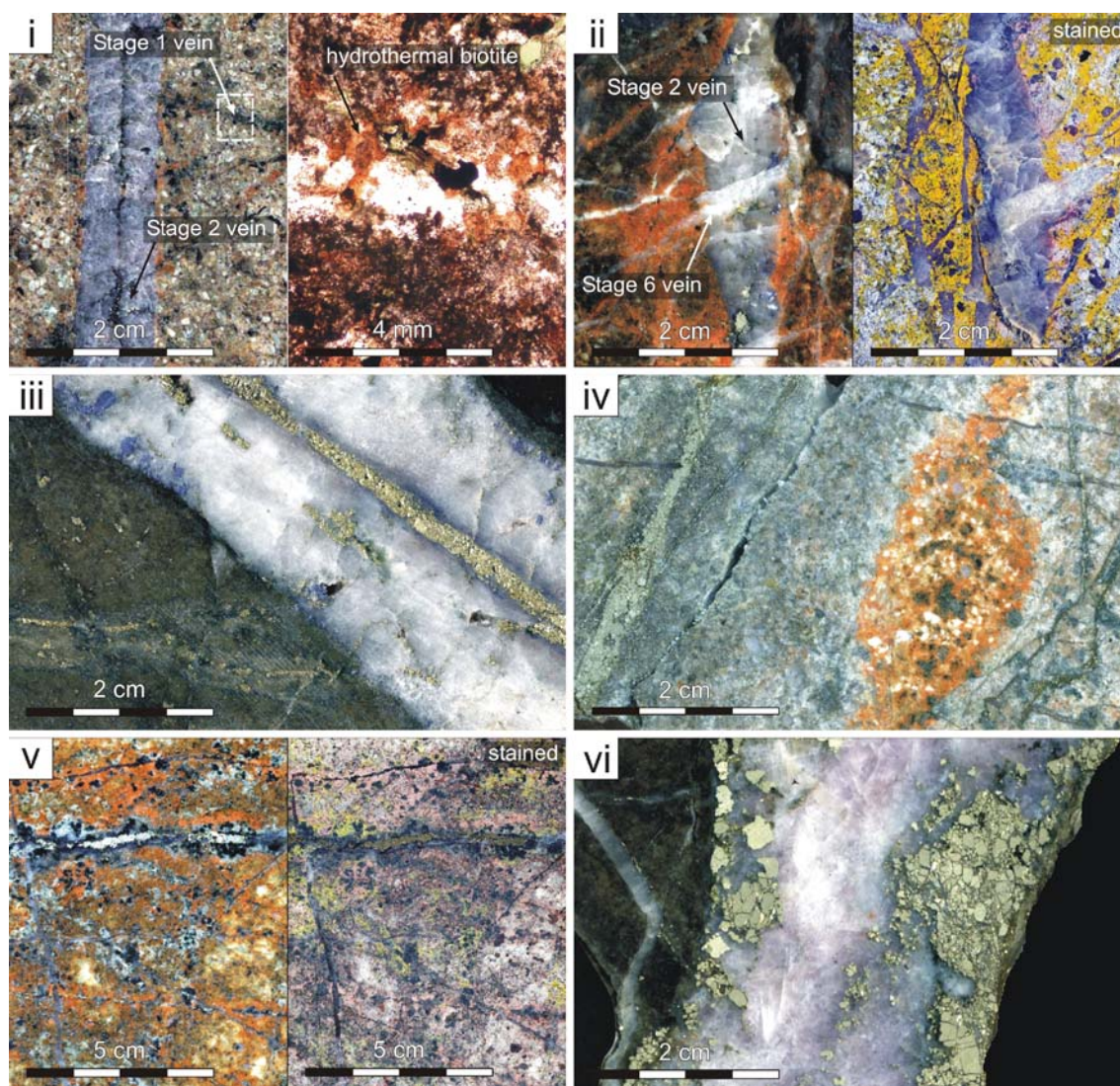


Fig. 8 Hand-specimen and thin-section photographs of representative vein types at Kameess South: (i) A 1- to 4-mm-thick stage 1 quartz–pyrite–biotite vein with a 3-mm-wide biotite alteration halo in granodiorite is cut by a stage 2 quartz–pyrite–chalcopyrite–magnetite–alkali feldspar vein. The photomicrograph, taken in transmitted plane-polarized light, is an enlargement of the area defined by the dashed box. Quartz and pyrite are intergrown with hydrothermal biotite. (ii) The unstained hand specimen shows a stage 2 quartz–pyrite–chalcopyrite–alkali feldspar–molybdenite vein and enveloping pink alkali feldspar alteration in granodiorite. Vein and alteration halo are cut by several stage 6 calcite veins. The matching sodium-cobaltinitrite-stained hand specimen highlights the alkali feldspar selvage to the vein. (iii) A stage 3 quartz–pyrite–chalcopyrite–molybdenite–chlorite–calcite vein cuts biotite-altered Takla Group

basalt. The vein contains a central seam of pyrite–molybdenite and contains 1- to 5-mm-diameter molybdenite grains along vein margins. Wall rock is altered to chlorite, quartz, and pyrite. This sample was used for Re–Os geochronology (sample KS-04-03-273, Table 1). (iv) A stage 3 pyrite–quartz–chalcopyrite–sericite–calcite vein and surrounding quartz–sericite–pyrite–chalcopyrite alteration replace hematite ± alkali feldspar ± biotite-altered granodiorite. (v) A type 4 pyrite–quartz–chlorite–calcite ± hematite stringer vein in granodiorite is surrounded by quartz, chlorite, and hematite. Staining with sodium cobaltinitrite indicates that the pink alteration mineral is not alkali feldspar (*right-hand photograph*). (vi) A type 5 anhydrite–pyrite–calcite vein cuts chlorite-altered Takla Group basalt. A 5-mm-thick type 6 calcite vein also cuts the basalt wall rock

Molybdenite from two stage 3 veins, hosted by granodiorite and Takla Group basalt on either side of the granodiorite–basalt contact (Fig. 4), has Re–Os model ages of 201.3 ± 1.2 and 201.1 ± 1.2 Ma, respectively (Table 1). These ages overlap the 199.6 ± 0.6 -Ma U–Pb zircon crystallization age (Mortensen et al. 1995) for the Maple Leaf granodiorite.

Late-stage mineralization veins: stage 4 veins

Stage 4 pyrite-rich stringer veins cut stage 3 veins in granodiorite and Takla Group basalt. Stage 4 veins are 1 to 4 mm thick and contain pyrite (70% to 95%), quartz (5% to 15%), sericite (<5%), chlorite (<5%), calcite (<3%), chalcopyrite (<3%), and hematite (<2%). Stage 4 veins

Table 1 Re–Os data and model ages for molybdenite from stage 3 Au–Cu–Mo-bearing veins at Kemess South

Sample number	Northing	Easting	Host rock	Sample description	Re (ppm)	$\pm 2\sigma$ (abs.)	^{187}Os (ppb)	$\pm 2\sigma$ (abs.)	Total common Os (pg)	Model age (Ma)	$\pm 2\sigma$ (abs.)
KS-04-03-117	6320046	635851	Maple Leaf granodiorite	Stage 3: qtz–py–cp–mt–bn–mo–ser \pm Au vein with phyllic alteration	4,609	30	9,730	40	<0.3	201.3	1.2
KS-04-03-273	6320046	635851	Takla Group basalt	Stage 3: qtz–py–cp–mt–bn–mo–chl \pm Au vein with phyllic alteration	3,106	20	6,550	26	6.7	201.1	1.2

abs absolute, *bn* bornite, *chl*, chlorite, *cp* chalcopyrite, *mo* molybdenite, *mt* magnetite, *py* pyrite, *qtz* quartz, *ser* sericite

are commonly surrounded by 1- to 3-cm-wide hematite \pm chlorite \pm sericite \pm quartz \pm pyrite alteration halos (Fig. 8 v). Three stage 4 veins mapped in the pit strike NW and dip 60° to 80° to the NE (Fig. 5 iv), but stage 4 veins were better observed in drill core, where they display irregular vein widths and more varied strike. Stage 4 veins and their associated phyllic or intermediate argillic alteration zones are responsible for late-stage Cu \pm Au mineralization at Kemess South.

Post-mineralization veins: stage 5, 6, and 7 veins

Stage 5 veins cut stage 4 veins in granodiorite and basalt and are the dominant vein type in basalt. Stage 5 veins are 0.5 to 5 cm thick and comprise anhydrite (60% to 80%), calcite (15% to 30%), and pyrite (5% to 10%). Anhydrite is commonly intergrown with 1- to 10-mm-diameter euhedral pyrite that cluster along vein margins but are also disseminated throughout the veins (Fig. 8 vi). Stage 5 veins are surrounded by <10-cm-wide anhydrite–pyrite alteration zones.

Stage 6 veins cut all existing vein types in granodiorite and basalt. Stage 6 veins are 1 to 5 mm thick, contain calcite (80%), zeolite (10%), quartz (3%), chlorite (3%), and pyrite (2%), and are surrounded by 1- to 5-cm-wide calcite alteration zones (Fig. 8 ii). Stage 6 veins commonly cut and reopen existing veins subparallel to vein margins.

Stage 7 veins cut all other vein types in granodiorite and basalt. Stage 7 veins are 1 to 3 mm thick, contain chlorite, and occur as randomly oriented microfracture networks. They commonly fill microfractures in fault-brecciated granodiorite.

Deposit-scale alteration

Hydrothermal alteration in granodiorite

Granodiorite is pervasively hydrothermally altered and displays multiple overprinting alteration events. Early-stage potassic alteration, associated with stage 1 and stage 2

veins, is only locally preserved in granodiorite. Where preserved, the potassic alteration zones are divided into alkali-feldspar-dominant (e.g., alkali feldspar–quartz–biotite–pyrite–chalcopyrite–magnetite), biotite-dominant (e.g., biotite–quartz–pyrite–magnetite–chalcopyrite), and transitional alteration zones (e.g., biotite–quartz–alkali feldspar–pyrite–chalcopyrite–magnetite). The alkali feldspar-dominant potassic alteration zones mainly occur distally to the granodiorite–basalt contact; the transitional zones occur more proximally to the contacts, and the biotite-dominant alteration zones occur along the contact with Takla Group basalt in the eastern area of the pit (Fig. 9 i). The local variation in mineral abundance for the potassic alteration event (i.e., alkali feldspar versus biotite) is probably a product of the reaction between a relatively homogeneous hydrothermal fluid and different wall rock compositions.

Phyllic alteration is the most common alteration style exhibited by the granodiorite and is widely distributed throughout the pit, but it is most intense to the west of the NW-striking 10180 fault (Fig. 9 i). In hand specimen, phyllic and intermediate argillic alteration selvages surround main- and late-stage veins (i.e., stage 3 and 4 veins) and replace potassic alteration zones. Phyllic alteration is expressed by sericite-dominant equilibrium alteration assemblages (i.e., sericite–quartz–pyrite–chalcopyrite–molybdenite), whereas intermediate argillic alteration mineral assemblages are chlorite-dominant (i.e., chlorite–quartz–pyrite–illite \pm chalcopyrite \pm molybdenite). Alkali feldspar-dominant potassic-altered granodiorite is mainly replaced by sericite-dominant phyllic alteration assemblages, whereas biotite-dominant potassic zones are replaced by intermediate argillic alteration zones.

Hydrothermal alteration in Takla Group basalt

Potassic alteration zones associated with stage 2 veins occur in basalt within 100 m of the granodiorite–basalt contact in the northeast wall (Fig. 9 i). Potassic alteration in basalt is defined by biotite–quartz–pyrite–magnetite alteration assemblages. Intermediate argillic alteration zones

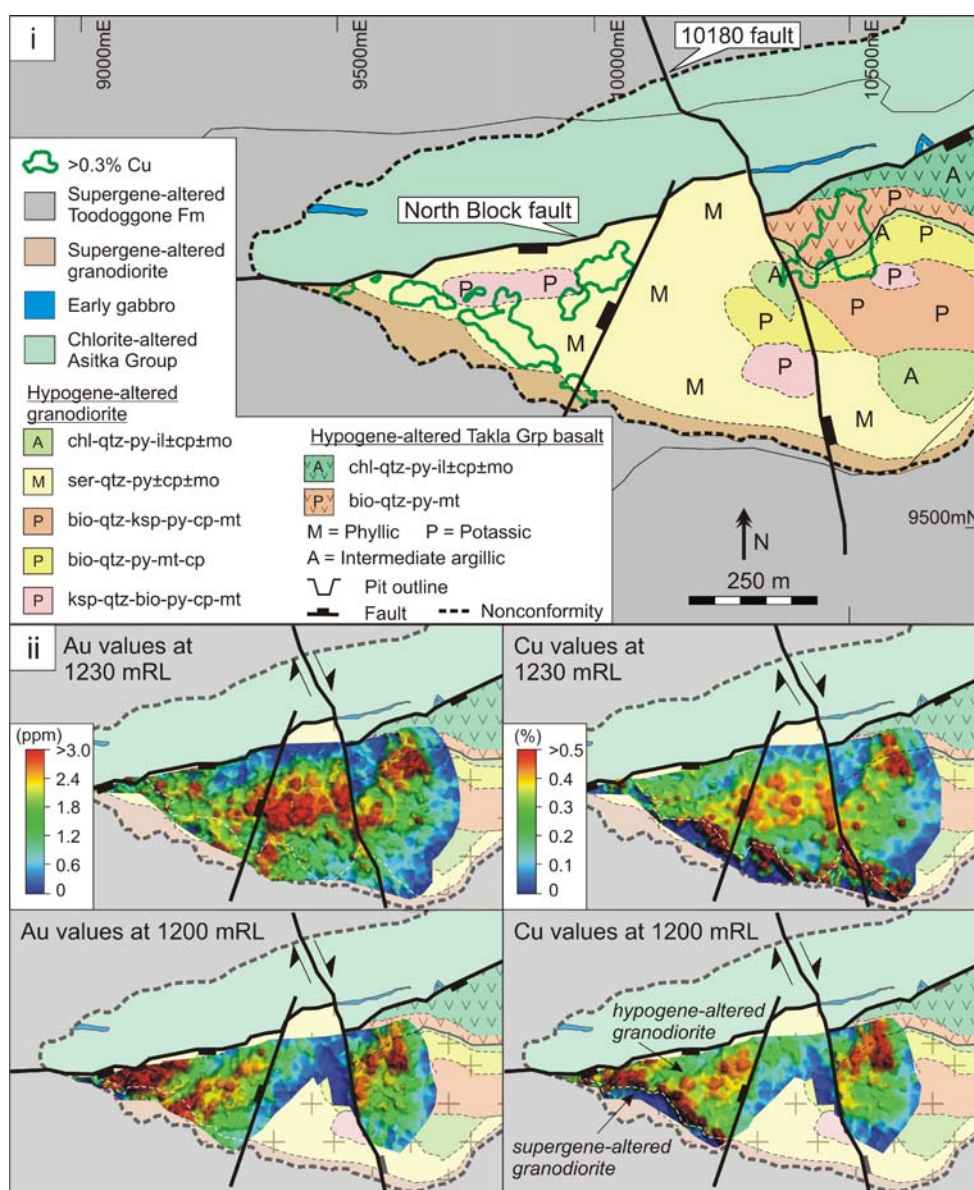


Fig. 9 Magmatic–hydrothermal alteration and the distribution of Au–Cu concentrations at Kemess South: (i) The simplified plan for the 1,200 mRL, about 100 m below the present surface, shows the distribution of potassic, phyllic, and intermediate argillic hydrothermal alteration zones in granodiorite and Takla Group basalt. Supergene alteration replaces hypogene alteration zones and defines an upper oxidized cap to the granodiorite. Overlying Toodoggone Formation rocks are also supergene-altered, whereas Asitka Group rocks to the north of the North Block fault are only weakly quartz-altered. Abbreviations: *bio*, biotite; *chl*, chlorite; *cp*, chalcopyrite; *il*, illite; *ksp*, alkali feldspar; *mo*, molybdenite; *mt*, magnetite; *py*, pyrite; *qtz*, quartz; *ser*, sericite. (ii) The horizontal plans for the 1,200 and 1,230 mRL show the spatial distribution of Au and Cu values. The

metal values are sourced from routine grade-control drilling in the pit with drill holes spaced about 5 m apart. Alteration zones for the 1,200 mRL are included in each plan for spatial reference. For both elevations, the distribution of Au and Cu are broadly comparable, although Cu is enriched relative to Au in the supergene alteration zones in granodiorite. The supergene–hypogene alteration transition in granodiorite is shown as a *dashed white line* in each plan. Northwest- and NE-trending normal faults truncate and displace the ore body. The faults define a central, Cu–Au-poor domain at the 1,200 mRL. Above the 1,200 mRL, this central block is Cu–Au rich. Hence, stratigraphically higher portions of the Cu–Au ore body have dropped either side of the central block, thereby juxtaposing different levels of the ore body via graben-and-horst-style faulting

associated with stage 3 and stage 4 veins are the dominant alteration style in basalt in areas more than 100 m from the granodiorite contact (Fig. 9 i). Intermediate argillic alteration is characterized by chlorite, quartz, illite, pyrite, chalcopyrite, and molybdenite.

Supergene alteration in granodiorite and Toodoggone Formation rocks

A 30-m-thick intensely weathered zone related to the circulation of supergene fluids blankets the upper margin

of the granodiorite, occurring in granodiorite and Toodoggone Formation rocks either side of the basal nonconformity (Figs. 4 and 9). The weathered zone in the granodiorite is divided into an upper, 10- to 30-m-thick, red-brown, hematite-limonite-rich “leached capping” (terminology after Sillitoe 2005) alteration zone and a lower, 1- to 3-m-thick, cream, kaolinite-rich zone. In both zones, igneous plagioclase and alkali feldspar laths are altered to kaolinite, whereas igneous hornblende and biotite and hydrothermal pyrite, chalcopyrite, and magnetite are mostly replaced by hematite and limonite in the upper zone. Disseminated chalcocite and bornite are reported to be hosted by granodiorite at the base of the supergene alteration zone (Rebagliati et al. 1995), whereas exotic native copper, malachite, and rare jarosite occur with hematite in the weathered basal conglomerate unit of the Toodoggone Formation (Fig. 4). Toodoggone Formation rocks located between the present surface and the basal nonconformity are less supergene-altered except where they are cut by moderate- to steep-dipping faults.

Spatial distribution of Cu–Au–Mo orebodies

Porphyry-style Au–Cu–Mo mineralization is mainly hosted by the Maple Leaf granodiorite, with minor ore zones hosted by Takla Group basalt within 50 m of the intrusive contact (Figs. 4 and 9 ii). Areas of granodiorite that contain the highest concentrations of hypogene Cu also commonly contain the highest Au values (Fig. 9 ii). The highest Cu–Au–Mo concentrations correspond to the greatest intensity of stage 3 veins and phyllic hydrothermal alteration. Unlike Cu and Au, Mo is not routinely analyzed during grade-control drilling and its distribution at Kemess South is less clearly defined. Where Mo grades are available, they are intimately associated with molybdenite-bearing stage 2 and 3 veins in granodiorite and basalt and broadly correspond to high Cu and Au values (Fig. 4). The northern extent of the granodiorite- and basalt-hosted ore body has been truncated by the North Block fault. The present location of the dismembered ore body to the north of the North Block Fault is uncertain, but it is likely that the ore body was exhumed and eroded.

Native copper grains (1- to 3-mm diameter) and malachite-filled fractures occur in 10-m-thick, exotic, low-tonnage Cu zones in the supergene-altered basal conglomerate unit of the Toodoggone Formation. Immediately below the nonconformity, the 30-m-thick leached capping in supergene-altered granodiorite contains low Cu values (<0.1% Cu). Copper concentrations increase below the supergene leached capping and locally peak at 0.75% Cu over 5 to 8 m at the supergene-hypogene alteration transition zone (Fig. 4). Gold and Mo are not remobilized as extensively as Cu (Fig. 4), although minor concentrations of detrital Au occur in meter-scale

depressions along the Toodoggone Formation basal nonconformity (G. Parrup: personal communication, 2005).

Northwest-striking normal–dextral faults and NE-striking normal faults displace the hypogene- and supergene-associated orebodies in granodiorite with displacements of about 50 m. At about 100 m below the present surface (i.e., the 1,200 mRL), NW- and NE-striking faults separate a Cu–Au-poor domain from flanking Cu–Au-rich domains in granodiorite (Fig. 9 ii). About 30 m above the 1,200 mRL, this central block is Cu–Au rich and the ore body is laterally continuous either side of the faults (Fig. 9 ii). Hence, in this example, NW- and NE-striking faults caused graben-and-horst-style block faulting of the ore body and resulted in the juxtapositioning of different levels of the ore body.

Fluid inclusion study on hydrothermal veins in granodiorite

Sample selection

Microthermometric analyses were performed on fluid inclusions in hydrothermal quartz from early- and main-stage veins to estimate temperature, pressure, and compositional conditions of the ore fluids during metal deposition. Early- (stages 1 and 2) and main-stage (stage 3) veins were selected because they host most of the Cu ± Au ± Mo mineralization and contain minerals that are amenable for microthermometric analysis. Late- and post-mineralization-stage veins (i.e., stage 4 to 7 veins) contain negligible Cu–Au–Mo mineralization and are not further discussed. Twelve doubly polished 80-μm-thick sections of stage 1, 2, and 3 veins were examined. From these, four sections of stage 1, 2, and 3 veins in granodiorite were selected for microthermometry. These veins were sampled from three diamond drill holes that are widely distributed throughout the granodiorite and from 61 to 291 m below the present surface. The veins are interpreted to represent the central region of the porphyry Cu–Au–Mo system.

Types of fluid inclusions

Fluid inclusions observed in quartz from all vein types are divided into primary, pseudosecondary, and secondary inclusions using the criteria of Roedder (1984) and based on their phase ratios at room temperature (25°C) and behavior during heating and freezing observations. Measured fluid inclusions are further subdivided into fluid inclusion assemblages (FIAs) using the criteria of Goldstein and Reynolds (1994). These FIAs are interpreted to represent coeval fluid inclusions that formed during a single fluid event.

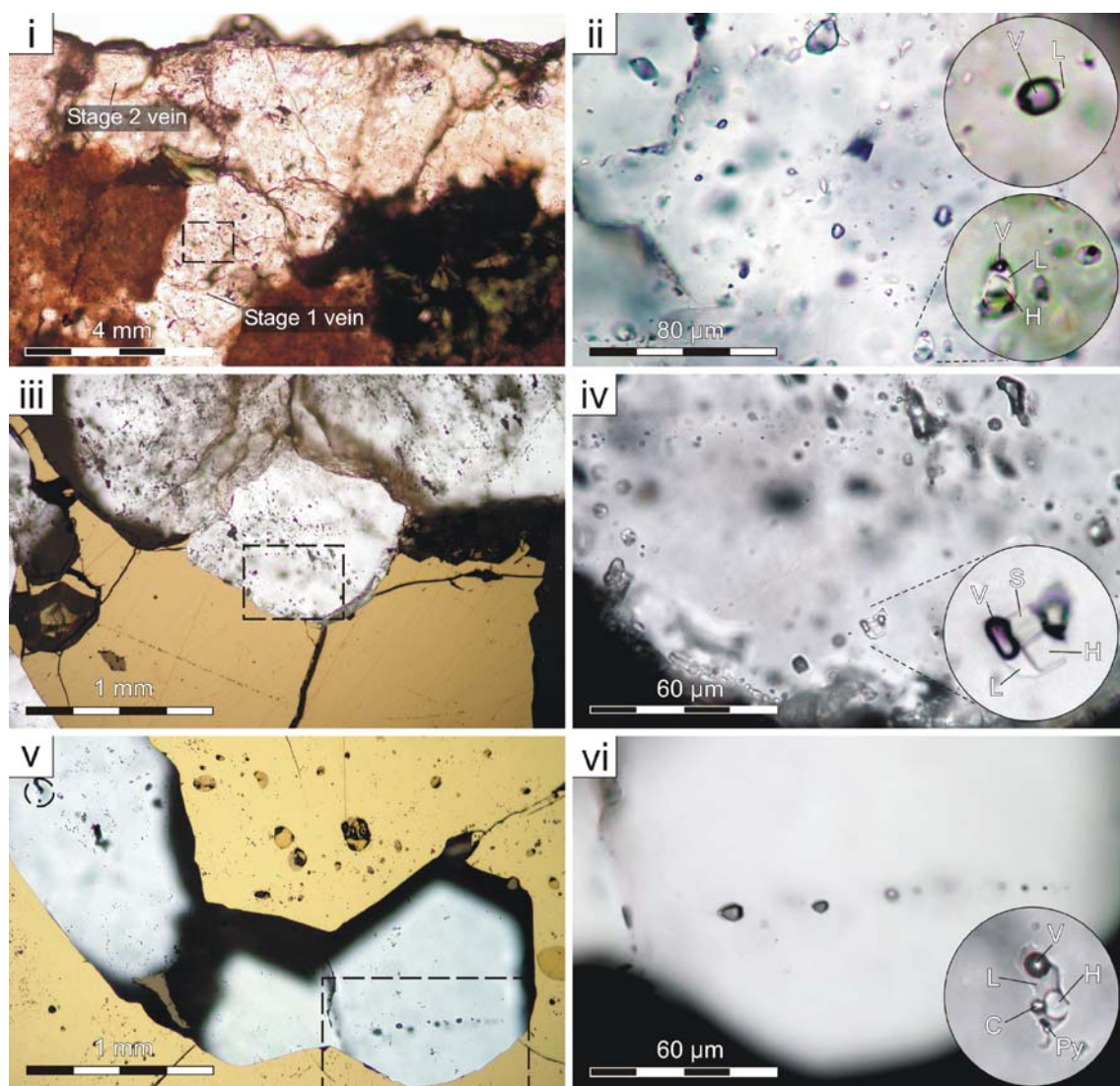


Fig. 10 The photographic plate shows petrographic features of stage 1, 2, and 3 veins and their fluid inclusions in granodiorite. All photographs were taken in transmitted plane-polarized light at 25°C, with the exception of photographs *iii* and *v*, which were taken in a combination of transmitted and reflected plane-polarized light. Abbreviations: C, carbonate mineral; H, halite; L, liquid; Py, pyrite; S, sylvite; V, vapor. (i) A 1- to 4-mm-thick stage 1 quartz–pyrite–biotite vein with a 3-mm-wide biotite alteration halo in granodiorite is cut by a stage 2 quartz–pyrite–chalcopyrite–magnetite–alkali feldspar vein. This section was prepared from the KS040-70 hand-specimen block shown in Fig. 8 i. The *dashed box* shows the position of photograph *ii*. (ii) Undeformed quartz with uniform extinction hosts randomly scattered coeval, type 1 brine-rich, multiphase, aqueous fluid inclusions and type 3 vapor-rich, two-phase, aqueous fluid inclusions. (iii) A stage 2 quartz–pyrite–chalcopyrite–molybdenite–magnetite–bismuthinite–alkali feldspar vein in granodiorite in sample

90-02-61.0. The quartz grain that borders pyrite is undeformed and displays uniform extinction. The *dashed box* shows the position of the magnified photograph in *iv*. (iv) Type 1 brine-rich, multiphase, aqueous inclusions and type 3 vapor-rich, two-phase, aqueous inclusions are scattered in the quartz. Brine-rich inclusions contain halite, sylvite, and a carbonate mineral. (v) A stage 3 pyrite–quartz–chalcopyrite–sericite–calcite–hematite vein in granodiorite (sample 90-02-100.3) contains pyrite with inclusions of chalcopyrite. The pyrite surrounds subhedral quartz that displays uniform extinction. A pseudosecondary fluid inclusion trail is shown in the *dashed box* area. (vi) The pseudosecondary fluid inclusion assemblage (FIA L in Table 2) includes several negative crystal-shaped type 3 vapor-rich aqueous inclusions that occur within the quartz grain. The *inset photograph* shows a 25-by-12-μm type 1 brine-rich aqueous inclusion that occurs in a nearby quartz grain (location indicated by the *dashed circle* in photograph *v*)

Primary and pseudosecondary fluid inclusions are divided based on their phase ratios at 25°C into three compositional types. Type 1 inclusions are brine-rich, multiphase (liquid + vapor + halite ± sylvite ± carbonate daughter ± opaque daughter minerals), aqueous inclusions that contain less than 10 vol.% vapor. Type 2 “mixed”

inclusions are multiphase (liquid + vapor ± halite) aqueous inclusions that display a diverse range of compositions, containing 10 to 80 vol.% vapor. Type 3 inclusions are vapor-rich, two-phase (liquid + vapor), aqueous inclusions that contain more than 80 vol.% vapor. Secondary fluid inclusions are common in all vein types and occur as two-

phase (liquid + vapor) fluid inclusion trails that cut quartz grain boundaries. Their timing with respect to the Cu–Au–Mo mineralization event is unclear and they are not discussed further. It is assumed that the volume and composition of primary and pseudosecondary fluid inclusions remained constant after entrapment because the granodiorite has not undergone significant metamorphism after crystallization and the quartz grains used in the study display uniform extinction in cross-polarized light and do not exhibit deformation or recrystallization textures.

Stage 1 quartz–pyrite–biotite–chalcopyrite–magnetite ± alkali feldspar veins contain 1- to 3-mm-diameter quartz grains that are unzoned and anhedral and are rimmed by biotite and pyrite (Fig. 8 i). Fluid inclusions in quartz are randomly scattered throughout the crystal and are interpreted to be primary or pseudosecondary (Fig. 10 i and ii). These inclusions include type 1 brine-rich (20%), type 2 mixed (40%), and type 3 vapor-rich inclusions (35%) and solid inclusions of opaque minerals that are identified as pyrite using reflected light microscopy (5%). Measured inclusions are equant, irregular- to negative crystal-shaped, 6 to 12 μm long (mean=9±2 μm , $n=12$), and 4 to 8 μm wide (mean=5±1 μm , $n=12$; Table 2).

Stage 2 quartz–pyrite–chalcopyrite–calcite–magnetite–alkali feldspar ± molybdenite ± gold veins cut stage 1 veins (e.g., sample KS040-70, Fig. 10 i) and contain 0.1- to 1.8-mm-diameter quartz grains that are unzoned and subhedral. Quartz grows from vein margins towards the center of the veins. Fluid inclusions in the quartz are randomly scattered (Fig. 10 iii and iv) or define trails that terminate at the margins of the grain; these inclusions are interpreted to be pseudosecondary and/or primary. These inclusions include type 1 brine-rich (25%), type 2 mixed (10%), type 3 vapor-rich (60%), and solid pyrite inclusions (5%). Measured inclusions are equant, irregular- to negative crystal-shaped, 3 to 30 μm long (mean=8±6 μm , $n=50$), and 2 to 12 μm wide (mean=6±4 μm , $n=50$).

Stage 3 pyrite–quartz–chalcopyrite–sericite–calcite ± chlorite ± molybdenite ± bismuthinite ± pyrrhotite ± apatite ± barite ± tennantite veins cut stage 2 veins at an oblique angle to or are subparallel to stage 2 vein margins. Quartz in stage 3 veins is 0.1–2 mm in diameter, anhedral, and unzoned. Quartz is commonly surrounded by pyrite and chalcopyrite and rimmed by sericite, chlorite, and molybdenite. Pyrite contains inclusions of euhedral sericite, chalcopyrite, bismuthinite, and molybdenite. Fluid inclusions in quartz occur as randomly scattered primary or pseudosecondary fluid inclusions. More rarely, the inclusions define pseudosecondary fluid inclusion trails that terminate at grain boundaries (Fig. 10 v and vi). These inclusions include type 1 brine-rich (40%), type 2 mixed (15%), and type 3 vapor-rich inclusions (40%) and inclusions of pyrite and chalcopyrite (5%). Locally,

pseudosecondary trails contain mostly type 3 vapor-rich inclusions (Fig. 10 vi). Measured inclusions are equant to elongate, irregular- to negative crystal-shaped, 3 to 30 μm long (mean=10±6 μm , $n=83$), and 2 to 25 μm wide (mean=7±6 μm , $n=83$).

Microthermometric results

Stage 1 veins

All measured fluid inclusions were cooled to –110°C and heated slowly to check for the presence of CO₂. Eutectic temperatures (T_e) and final ice melting temperatures (T_m) were not observed in type 3 vapor-rich inclusions due to the difficulty in perceiving the first and final melting of ice. No CO₂ was detected in any fluid inclusion. Type 3 vapor-rich inclusions have vapor homogenization temperatures (T_h ; to the vapor phase) of 372°C and 388°C ($n=2$). Type 1 brine-rich inclusions have a T_h range (to the liquid phase) from 142°C to 229°C (mean=198±41°C, $n=5$) and total homogenization temperatures (T_h total), indicated by the dissolution of the halite daughter crystal, that range from 225°C to 346°C (mean=277±58°C, $n=5$; Table 2). Salinities calculated using the dissolution temperatures of halite indicate a range from 33.2 to 42.0 equiv. wt.% NaCl (mean=36.9±4.2 equiv. wt.% NaCl, $n=5$). The wide range of T_h total estimates and their clustering in two groups suggest that these inclusions might record two separate fluid events, contradicting initial petrologic interpretations.

Stage 2 veins

Eutectic temperatures (T_e) and T_m were not observed in type 3 vapor-rich inclusions due to the difficulty in observing the first and final melting of ice. No CO₂ was detected in any fluid inclusion. Type 3 vapor-rich inclusions have T_h (to the vapor phase) of 341°C and 418°C ($n=2$). Type 1 saline inclusions have a wide T_h range (to the liquid phase) from 91°C to 364°C (mean=237±70°C, $n=22$) and T_h total, indicated by the dissolution of the halite daughter crystal, that range from 324°C to 463°C (mean=379±62°C, $n=22$; Table 2). Salinities calculated using the dissolution temperatures for halite indicate a range from 40.6 to 54.9 equiv. wt.% NaCl (mean=45.8±6.2 equiv. wt.% NaCl, $n=22$). Dissolution temperatures for sylvite daughter crystals range from 161°C to 173°C (mean=167±8°C, $n=3$).

Stage 3 veins

Eutectic temperatures (T_e) for type 3 vapor-rich inclusions are –26.0°C and –22.0°C ($n=2$), whereas T_m range from –9.0 to –5.6 (mean=–7.0±1.5°C, $n=6$). No CO₂ was detected in any fluid inclusion. The T_e is below the eutectic

Table 2 Summary of microthermometric data from Kerness South veins

FIA	Sample chip	Petrographic description at 25°C	Type of inclusion	Vol.% of vapor	Th (°C) (α - γ)	Tm halite or Tm ice (°C)	Salinity (equivalent weight percent NaCl)
Stage 1 veins: quartz-pyrite-biotite-chalcopyrite							
3.X ($n=3$) KS040-70-C3 Quartz hosts randomly arranged, equant, brine-rich, pseudosecondary inclusions that contain a halite daughter crystal							
E ($n=2$)	KS040-70-C4	Quartz hosts randomly arranged, irregular- to negative crystal-shaped, brine-rich, pseudosecondary inclusions that contain a halite daughter crystal and a second translucent mineral (?carbonate)	Brine rich	5 to 10	229 (L)	332 to 346	40.8 to 42.0
Stage 2 veins: quartz-chalcopyrite-pyrite-alkali feldspar							
F ($n=3$)	KS040-70-C6	Quartz hosts randomly arranged, equant, irregular-shaped, brine-rich, pseudosecondary inclusions that contain a halite daughter crystal, a second translucent mineral (?carbonate), and chalcopyrite	Brine rich	5 to 10	91 to 134 (L)	324 to 366	40.6 to 44.0
G ($n=2$)	KS040-70-C7	Quartz hosts randomly arranged, equant, irregular-shaped, brine-rich, pseudosecondary inclusions that contain a halite daughter crystal, a second translucent mineral (?carbonate), sylvite, and chalcopyrite	Brine-rich	5	176 to 202 (L)	332 to 430	40.8 to 50.9
J ($n=7$)	KS040-48-C4	Quartz along the vein margin hosts randomly arranged, equant, irregular- to negative crystal-shaped, brine-rich, pseudosecondary inclusions that contain a halite daughter crystal, a second translucent mineral (?carbonate), sylvite, and chalcopyrite	Brine rich	5 to 10	218 to 251 (L)	447 to 463	52.9 to 54.9
K ($n=3$)	KS040-48-C5	Quartz along the vein margin hosts randomly arranged, equant, irregular- to negative crystal-shaped, brine-rich, pseudosecondary inclusions that contain a halite daughter crystal, a second translucent mineral (?carbonate), and pyrite	Brine rich	5 to 10	170 to 224 (L)	403 to 418	47.8 to 49.5
Q ($n=5$)	90-02-61.0-C5	Quartz that is rimmed by pyrite and chalcopyrite hosts randomly arranged, equant, irregular-shaped, brine-rich, pseudosecondary inclusions that contain a halite daughter crystal, a second translucent mineral (?carbonate), and pyrite	Brine rich	5 to 10	269 to 288 (L)	365	43.8
R ($n=2$)	90-02-61.0-C2	Quartz that is rimmed by pyrite hosts randomly arranged, equant, irregular-shaped, brine-rich, pseudosecondary inclusions that contain halite and sylvite daughter crystals	Brine rich	8 to 10	306 to 364 (L)	443 to 460	52.4 to 54.5
Stage 3 veins: pyrite-quartz-chalcopyrite-magnetite-bismuthinite-molybdenite-pyrrhotite-bornite-carbonate-chlorite \pm sericite \pm apatite							
B ($n=4$)	KS040-70-C1	Quartz grain that is encircled by pyrite hosts randomly arranged, equant, irregular-shaped, brine-rich, pseudosecondary inclusions that contain halite and sylvite daughter crystals	Brine rich	5 to 10	223 to 263 (L)	288 to 391	37.3 to 46.5
D ($n=2$)	KS040-70-C2	Quartz grain that is encircled by pyrite hosts randomly arranged, equant, irregular-shaped, chalcopyrite and brine-rich primary inclusions that contain halite and sylvite daughter crystals, a translucent mineral (?carbonate), and pyrite and chalcopyrite	Brine rich	5 to 10	215 to 224 (L)	422 to 460	49.9 to 54.5
2.D ($n=3$)	KS040-70-C2	Quartz grain that is encircled by pyrite, chalcopyrite, and magnetite hosts randomly arranged, equant, irregular- to negative crystal-shaped, brine-rich, primary inclusions that contain halite and sylvite daughter crystals and a translucent mineral (?carbonate)	Brine rich	5 to 8	164 to 167 (L)	315 to 391	39.4 to 46.5
H ($n=2$)	KS040-48-C2	Quartz grain that is rimmed by pyrite hosts randomly arranged, equant, irregular-shaped, brine-rich, primary inclusions that contain a halite daughter crystal and pyrite	Brine rich	5 to 10	171 to 181 (L)	366 to 377	43.9 to 45.0
L ($n=2$)	90-02-110.3-C1	Quartz grain that is encircled by pyrite hosts a trail of pseudosecondary, negative crystal-shaped, vapor-rich inclusions	Vapor rich	95	363 (V)	-9.6	13.5
M ($n=5$)	90-02-110.3-C1	Quartz grain that is encircled by pyrite hosts randomly arranged, equant, irregular- to negative crystal-shaped, brine-rich, primary inclusions that contain halite and sylvite daughter crystals, a translucent mineral (?carbonate), and pyrite and chalcopyrite	Brine-rich	5 to 10	271 to 316 (L)	363 to 412	43.7 to 48.7
N ($n=6$)	90-02-110.3-C2	Quartz grain that is encircled by pyrite hosts randomly arranged, equant, irregular- to negative crystal-shaped, brine-rich, primary inclusions that contain halite and sylvite daughter	Brine rich	5	234 to 290 (L)	317 to 451	42.2 to 53.4

O ($n=2$)	90-02-110.3-C4	crystals, a translucent mineral (?carbonate), and pyrite and chalcopyrite Quartz grain that is encircled by pyrite hosts randomly arranged, equant, negative crystal-shaped, brine-rich, primary inclusions that contain halite and sylvite daughter crystals, a translucent mineral (?carbonate), and pyrite and chalcopyrite	Brine rich	5 to 8	242 (L)	376 to 435	45.0 to 51.4
O.2 ($n=2$)	90-02-110.3-C4	Quartz grain that is encircled by pyrite hosts randomly arranged, negative crystal-shaped, vapor-rich inclusions	Vapor rich	5 to 8	358 to 400 (V)	-6.0 to -5.6	8.6 to 9.2
P ($n=5$)	90-02-110.3-C5	Quartz grain that is rimmed by pyrite hosts randomly arranged, equant, negative crystal-shaped, brine-rich, primary inclusions that contain a halite daughter crystal, a translucent mineral (?carbonate), and pyrite	Brine rich	5 to 10	202 to 253 (L)	294 to 380	37.7 to 45.3

Microthermometric measurements were conducted on a Linkam THMSG 600 stage at the University of British Columbia. Precision is $\pm 0.2^\circ\text{C}$ for temperatures below $+30^\circ\text{C}$ and $\pm 3.0^\circ\text{C}$ for temperatures above $+30^\circ\text{C}$. Salinities (equivalent weight percent NaCl) were calculated using the MacFlinCor program (Brown and Hagemann 1995), which uses the Bodnar and Vityk (1994) and Bodnar et al. (1985) equations of state for the H_2O –NaCl–KCl system

temperature for the H_2O –NaCl system (i.e., -20.8°C) and indicates the presence of dissolved salts other than NaCl (Shepherd et al. 1985). Final ice melting temperatures correspond to calculated salinities of 8.7 to 12.9 equiv. wt.% NaCl (mean= 10.4 ± 1.9 equiv. wt.% NaCl, $n=6$). Type 3 vapor-rich inclusions have T_h (to the vapor phase) that range from about 358°C to 500°C (mean= $433\pm 65^\circ\text{C}$, $n=6$). Type 1 brine-rich inclusions have a T_h range (to the liquid phase) from 164°C to 316°C (mean= $238\pm 44^\circ\text{C}$, $n=33$) and T_h total, indicated by the dissolution of the halite daughter crystal, that range from 288°C to 460°C (mean= $380\pm 43^\circ\text{C}$, $n=33$; Table 2). Salinities calculated using the dissolution temperatures of halite indicate a range from 37.3 to 54.5 equiv. wt.% NaCl (mean= 45.7 ± 4.4 equiv. wt.% NaCl, $n=33$). Dissolution temperatures for sylvite daughter crystals range from 98°C to 240°C (mean= $187\pm 46^\circ\text{C}$, $n=9$).

Stable isotope results

Sulfur isotope data for sulfide and sulfate minerals

Pyrite, chalcopyrite, and anhydrite were analyzed from veins hosted by granodiorite and basalt. The samples were collected from depths of 44 to 333 m below the present surface and from three diamond drill holes that are spaced widely apart in the deposit. The samples were collected from the central portion of the porphyry system. All sulfur isotope values are broadly similar for early- (stage 2), main- (stage 3), late- (stage 4), and post-mineralization-stage (stage 5) veins. Stage 2 veins have $\delta^{34}\text{S}$ values for pyrite that range from 0.3‰ to 2.9‰ (mean= $1.3\pm 0.8\%$, $n=7$; Table 3). Stage 3 veins have $\delta^{34}\text{S}$ values for pyrite that range from -0.3% to 1.6‰ (mean= $0.8\pm 0.8\%$, $n=6$), whereas $\delta^{34}\text{S}$ values for broadly contemporaneous chalcopyrite are -0.1% and 1.1‰ ($n=2$). Stage 4 veins have $\delta^{34}\text{S}$ values for pyrite that range from 0.0‰ to 2.4‰ (mean= $1.2\pm 1.0\%$, $n=5$). Stage 5 veins have $\delta^{34}\text{S}$ values for pyrite that range from 0.9‰ to 1.9‰ (mean= $1.4\pm 0.4\%$, $n=4$), whereas $\delta^{34}\text{S}$ values for coeval anhydrite range from 11.0‰ to 13.4‰ (mean= $12.6\pm 1.0\%$, $n=6$). The Δ values for anhydrite–pyrite pairs range from 9.7‰ to 12.5‰ (mean= $11.3\pm 1.2\%$, $n=4$).

Oxygen and carbon isotope data

Oxygen and carbon isotope values were determined for calcite from early- (stage 2), main- (stage 3), and post-mineralization-stage (stage 6) veins. The veins are hosted by granodiorite and basalt and were sampled from depths between 18 and 282 m below the present surface from three diamond drill holes spaced widely apart in the deposit. The

Table 3 Sulfur isotope data from vein sulfides at Kerness South

Sample number	Northing	Easting	Host rock	Sample description	$\delta^{34}\text{S}$ (‰) V-CDT				
					py	cp	anh	$\Delta_{\text{anh-py}}$	T (°C)
KE-04-02-273.3-py	6320222	635448	Maple Leaf granodiorite	Stage 2: qtz–bio–py–cp–ksp \pm mo \pm Au vein with potassic alteration	2.9				
KE-04-02-284.5-py	6320222	635448	Maple Leaf granodiorite	Stage 2: qtz–bio–py–cp–ksp \pm mo \pm Au vein with potassic alteration	1.1				
KS-04-03-102.7-py	6320046	635851	Maple Leaf granodiorite	Stage 2: qtz–bio–py–cp–ksp \pm mo \pm Au vein with potassic alteration	0.3				
KS-04-03-117.4-py	6320046	635851	Maple Leaf granodiorite	Stage 2: qtz–bio–py–cp–ksp \pm mo \pm Au vein with potassic alteration	1.0				
90-02-110.3-py	6320313	636697	Maple Leaf granodiorite	Stage 2: qtz–bio–py–cp–ksp \pm mo \pm Au vein with potassic alteration	1.4				
90-02-44.5-py	6320313	636697	Maple Leaf granodiorite	Stage 2: qtz–bio–py–cp–ksp \pm mo \pm Au vein with potassic alteration	1.4				
KS-04-03-262.1-py	6320046	635851	Takla Group basalt	Stage 2: qtz–bio–py–cp–ksp \pm mo \pm Au vein with potassic alteration	0.8				
KE-04-02-290.5-py	6320222	635448	Maple Leaf granodiorite	Stage 3: qtz–py–cp–mt–mo–chl \pm Au vein with phyllic alteration	1.6				
KE-04-02-302.0-cp	6320222	635448	Maple Leaf granodiorite	Stage 3: qtz–py–cp–mt–mo–chl \pm Au vein with phyllic alteration		–0.1			
90-02-185.0-cp	6320313	636697	Takla Group basalt	Stage 3: qtz–py–cp–mt–mo–chl \pm Au vein with phyllic alteration	–0.3				
KS-04-03-156.2-py	6320046	635851	Maple Leaf granodiorite	Stage 3: qtz–py–cp–mt–mo–chl \pm Au vein with phyllic alteration	1.4	1.1			
KS-04-03-198.3B-py	6320046	635851	Maple Leaf granodiorite	Stage 3: qtz–py–cp–mt–mo–chl \pm Au vein with phyllic alteration	1.2				
KS-04-03-248.5B-py	6320046	635851	Maple Leaf granodiorite	Stage 3: qtz–py–cp–mt–mo–chl \pm Au vein with phyllic alteration	0.1				
KS-04-03-273.5-py	6320046	635851	Takla Group basalt	Stage 3: qtz–py–cp–mt–mo–chl \pm Au vein with phyllic alteration	1.0				
KS-04-03-140.0-py	6320046	635851	Maple Leaf granodiorite	Stage 4: py–qtz–ser stringer vein with phyllic alteration	1.3				
KS-04-03-296.7-py	6320046	635851	Maple Leaf granodiorite	Stage 4: py–qtz–ser stringer vein with phyllic alteration	2.4				
KS-04-03-330.2-py	6320046	635851	Maple Leaf granodiorite	Stage 4: py–qtz–ser stringer vein with phyllic alteration	2.0				
KE-04-02-332.2-py	6320046	635851	Maple Leaf granodiorite	Stage 4: py–qtz–ser stringer vein with phyllic alteration	0.3				
90-02-220.0-py	6320313	636697	Takla Group basalt	Stage 4: py–qtz–ser stringer vein with phyllic alteration	0.0				
90-02-225.0-py	6320313	636697	Takla Group basalt	Stage 5: anh–py vein with anhydrite alteration	1.9		13.3	11.5	473
KS-04-03-304.0-py	6320046	635851	Takla Group basalt	Stage 5: anh–py vein with anhydrite alteration	1.3		12.9	11.6	470
KS-04-03-309.5-py	6320046	635851	Takla Group basalt	Stage 5: anh–py vein with anhydrite alteration	1.3		11.0	9.7	542
KS-04-03-310.8-py	6320046	635851	Takla Group basalt	Stage 5: anh–py vein with anhydrite alteration	0.9		13.4	12.5	440
90-02-207.0-anh	6320313	636697	Takla Group basalt	Stage 5: anh–py vein with anhydrite alteration			13.1		
KS-04-03-289.9-anh	6320046	635851	Takla Group basalt	Stage 5: anh–py vein with anhydrite alteration			12.0		

Purity was greater than 98% for pyrite and chalcopyrite and 99% for anhydrite. The $\delta^{34}\text{S}$ data are reported in per mil, relative to Cañon Diablo Troilite (CDT), with relative analytical accuracy and precision of $\pm 0.3\text{‰}$

anh anhydrite, *bio* biotite, *chl* chlorite, *cp* chalcopyrite, *ksp* alkali feldspar, *mo* molybdenite, *mt* magnetite, *py* pyrite, *qtz* quartz, *ser* sericite

vein samples are considered to be representative of the center of the porphyry system. Calcite from weakly quartz–pyrite-altered coral-bearing Asitka Group limestone was also analyzed. Stage 2 veins have $\delta^{18}\text{O}$ values of 11.6‰

and 12.6‰ ($n=2$) and $\delta^{13}\text{C}$ values of 0.4‰ and 0.5‰ ($n=2$; Table 4). Stage 3 veins have $\delta^{18}\text{O}$ values that range from 9.7‰ to 12.5‰ (mean = $10.9 \pm 1.3\text{‰}$, $n=4$) and $\delta^{13}\text{C}$ values of -3.8‰ to 0.1‰ (mean = $-1.8 \pm 1.6\text{‰}$, $n=4$). Stage

Table 4 Carbon and oxygen isotope data for calcite from veins and limestone at Kemess South

Sample number	Northing	Easting	Host rock	Sample description	$\delta^{13}\text{C}$ (‰) V-PDB	$\delta^{18}\text{O}$ (‰) V-SMOW
KS-04-03-262.1	6320046	635851	Takla Group basalt	Stage 2: qtz–bio–py–cp–ksp–ca \pm mo \pm Au vein with potassic alteration	0.4	12.6
90-02-44.5	6320313	636697	Maple Leaf granodiorite	Stage 2: qtz–bio–py–cp–ksp–ca \pm mo \pm Au vein with potassic alteration	0.5	11.6
90-02-185.0	6320313	636697	Takla Group basalt	Stage 3: qtz–py–cp–mt–mo–chl–ca \pm Au vein with phyllic alteration	–1.3	9.7
KS-04-03-156.2	6320046	635851	Maple Leaf granodiorite	Stage 3: qtz–py–cp–mt–mo–chl–ca \pm Au vein with phyllic alteration	–2.3	11.3
KS-04-03-273.5	6320046	635851	Takla Group basalt	Stage 3: qtz–py–cp–mt–mo–chl–ca \pm Au vein with phyllic alteration	0.1	12.5
KS-04-03-111.2	6320046	635851	Maple Leaf granodiorite	Stage 3: qtz–py–cp–mt–mo–chl–ca \pm Au vein with phyllic alteration	–3.8	10.0
KS-04-03-144.0	6320046	635851	Maple Leaf granodiorite	Stage 6: calcite vein with calcite alteration	–0.9	13.6
KE-04-02-282B	6320036	635452	Maple Leaf granodiorite	Stage 6: calcite vein with calcite alteration	0.3	12.4
90-02-18.8	6320313	636697	Maple Leaf granodiorite	Stage 6: calcite vein with calcite alteration	–0.1	14.7
90-02-187.0	6320313	636697	Maple Leaf granodiorite	Stage 6: calcite vein with calcite alteration	0.0	12.0
KE-04-02-381.5	6320036	635452	Asitka Group limestone	Least-altered limestone country rock	0.4	13.1

The $\delta^{13}\text{C}$ and $\delta^{18}\text{O}$ data are reported in per mil relative to the Vienna Pee Dee Belemnite (V-PDB) and the Vienna Standard Mean Ocean Water (V-SMOW) standards, respectively. Relative analytical accuracy and precision for sample analyses is $\pm 0.2\text{‰}$ (Macdonald and Spooner 1981; Brown and Hagemann 1995; Bodnar and Vityk 1994; Bodnar et al. 1985)

bio biotite, *ca* calcite, *chl* chlorite, *cp* chalcopyrite, *ksp* alkali feldspar, *mo* molybdenite, *mt* magnetite, *py* pyrite, *qtz* quartz, *ser* sericite

6 veins have $\delta^{18}\text{O}$ values that range from 12.0‰ to 14.8‰ (mean = $13.2 \pm 1.2\text{‰}$, $n=4$) and $\delta^{13}\text{C}$ values of -0.9‰ to 0.3‰ (mean = $-0.2 \pm 0.5\text{‰}$, $n=4$). One weakly altered Asitka Group limestone sample has a $\delta^{18}\text{O}$ value of 13.1‰ and a $\delta^{13}\text{C}$ value of 0.4‰.

Physicochemical conditions of the Kemess south hydrothermal ore fluids

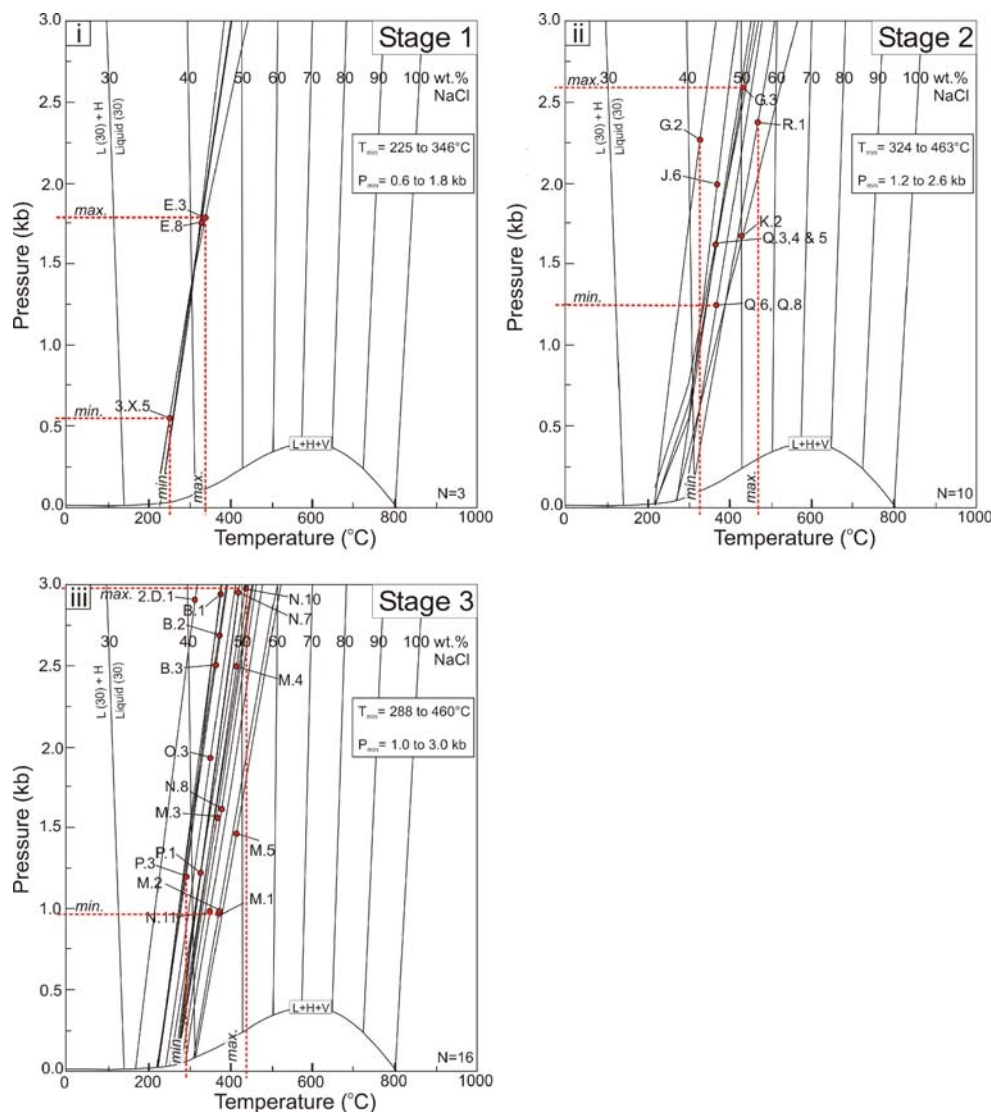
Early- (stages 1 and 2) and main-stage (stage 3) veins host primary or pseudosecondary fluid inclusions that include type 1 brine-rich and type 3 vapor-rich inclusions. In all vein stages at Kemess South, the type 1 brine-rich inclusions homogenize by halite dissolution at temperatures higher than the vapor-bubble disappearance temperature. Consequently, these type 1 brine-rich and type 3 vapor-rich fluid inclusions cannot be immiscible pairs trapped at equilibrium (Bodnar 1994; Roedder and Bodnar 1980). Hence, measured total homogenization temperatures represent minimum trapping temperature estimates. The data suggest that the brine- and vapor-rich inclusions formed during the immiscible interaction of at least two fluids of different composition and origin, resulting in the heterogeneous (non-equilibrium) trapping of brine- and vapor-rich fluids. Water leakage from brine-rich inclusions after trapping might also contribute to the overwhelming tendency for type 1 brine-rich inclusions to homogenize by halite dissolution.

Total homogenization temperatures for primary or pseudosecondary fluid inclusions in early-stage (stage 1) quartz–pyrite–biotite–chalcopyrite–magnetite \pm alkali feldspar veins have a range of 225°C to 346°C ($n=3$) and a corresponding pressure range of 0.6 to 1.8 kbar (Fig. 11 i). These temperatures and pressures are minimum estimates; the true trapping T–P conditions lie somewhere higher along the projected isochores. Assuming lithostatic fluid pressure conditions and a pressure gradient of 3.3 km/1 kbar (Hagemann and Brown 1996), pressures of 0.6 kbar correspond to minimum formational depths of 2.0 km for stage 1 veins.

Early-stage (stage 2) quartz–pyrite–chalcopyrite–calcite–magnetite–alkali feldspar \pm molybdenite \pm gold veins host primary or pseudosecondary fluid inclusions that have total homogenization temperatures that range from 324°C to 463°C ($n=10$), which correspond to a pressure range of 1.2 to 2.6 kbar (Fig. 11 ii). Assuming lithostatic fluid pressure conditions and a pressure gradient of 3.3 km/1 kbar (Hagemann and Brown 1996), the 1.2-kbar minimum trapping pressure corresponds to a minimum formational depth of 4.0 km for stage 2 veins.

Main-stage (stage 3) pyrite–quartz–chalcopyrite–sericite–chlorite–calcite \pm molybdenite \pm bismuthinite \pm pyrrhotite \pm apatite \pm barite \pm tennantite veins contain primary or pseudosecondary fluid inclusions that have total homogenization temperatures that range from 288°C to 460°C ($n=16$), which correspond to a large pressure range of 1.0 to

Fig. 11 The pressure–temperature diagram shows calculated isochores and P–T trapping condition estimates for early- (stages 1 and 2) and late-stage (Stage 3) veins at Kerness South. Isochores for primary/pseudosecondary type 1 brine-rich fluid inclusions were calculated using the MacFlinCor program (Brown and Hagemann 1995) and the Bodnar and Vityk (1994) equation of state for the H₂O–NaCl–KCl system



3.0 kbar (Fig. 11 iii). Assuming lithostatic fluid pressure conditions and a pressure gradient of 3.3 km/1 kbar (Hagemann and Brown 1996), the 1.0-kbar minimum trapping pressure corresponds to a minimum formational depth of 3.3 km for stage 3 veins.

Late-stage (stage 4) pyrite–quartz ± sericite ± chlorite ± chalcopyrite ± hematite veins do not have any temperature–pressure constraints. Post-mineralization-stage (stage 5) anhydrite–pyrite ± calcite veins contain coeval anhydrite and pyrite in apparent textural equilibrium (Fig. 8 vi). Using $\delta^{34}\text{S}$ values for anhydrite and pyrite and the sulfur isotope fractionation equation of Ohmoto and Lasaga (1982), anhydrite–pyrite equilibrium mineral pair temperatures for stage 5 veins range from 440°C to 542°C (average = $481 \pm 43^\circ\text{C}$, $n=4$; Table 3). This temperature range for stage 5 veins is higher than temperature ranges for early- to main-stage veins and suggests the involvement of a second hot magmatic or hydrothermal fluid or that samples of anhydrite and pyrite were not actually in equilibrium. Precise

temperature estimates for the formation of stage 6 calcite ± zeolite ± quartz ± chlorite ± pyrite veins were not determined; however, an approximate temperature of 200°C is indicated by the stability of zeolite (Turner 1981).

Constraints on the source of sulfur, carbon, and metals in the hydrothermal ore fluids

Sulfur isotope constraints

Early- (stage 2), main- (stage 3), late- (stage 4), and post-mineralization-stage (stage 5) veins display overlapping $\delta^{34}\text{S}$ values for pyrite and chalcopyrite that range from -0.3‰ to 2.9‰ (Table 3, Fig. 12). Using average hydrothermal fluid temperature estimates determined from fluid inclusion studies on early- to post-mineralization-stage veins as well as equilibrium sulfide mineral–H₂S isotope factors for pyrite and chalcopyrite (Ohmoto and Rye 1979),

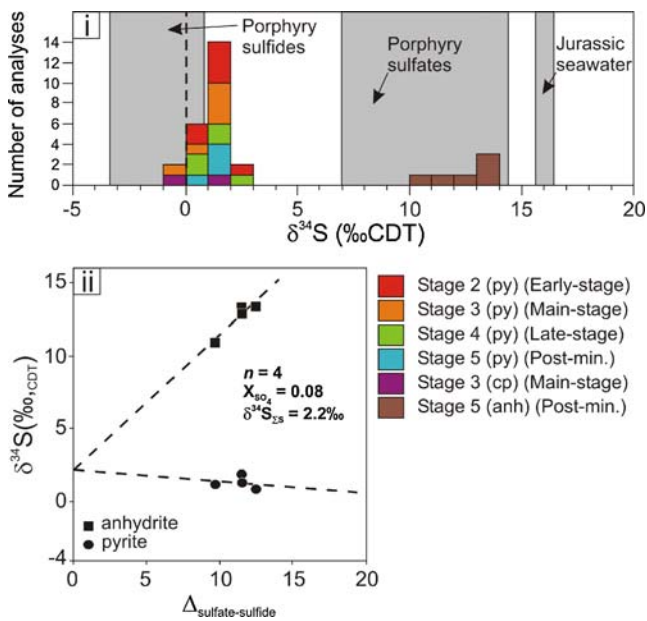


Fig. 12 Sulfur isotope values for pyrite, chalcopyrite, sphalerite, and anhydrite from Kames South. (i) The range of $\delta^{34}\text{S}$ values for sulfide and sulfate minerals from early-, main-, late-, and post-mineralization-stage veins overlap the typical $\delta^{34}\text{S}$ ranges for porphyry-related sulfide and sulfate minerals, as defined by Rollinson (1993). The $\delta^{34}\text{S}$ range for Jurassic seawater sulfur (Claypool et al. 1980) is also shown for reference. (ii) $\delta^{34}\text{S}$ versus $\Delta^{34}\text{S}_{\text{sulfate-sulfide}}$ ratios for coexisting sulfate-sulfide mineral pairs from post-mineralization-stage (stage 5) anhydrite-pyrite veins

calculated $\delta^{34}\text{S}_{\text{H}_2\text{S}}$ values for these sulfide minerals range from -1.3‰ to 2.0‰ (mean = $0.2 \pm 0.8\text{‰}$, $n = 24$). Although the temperature estimates used above are approximate values for the vein stages at Kames South, they are considered to be reasonable because a variation in temperature of $\pm 100^\circ\text{C}$ translates to a negligible difference in $\delta^{34}\text{S}_{\text{H}_2\text{S}}$ values of $< 0.4\text{‰}$. The Kames South $\delta^{34}\text{S}_{\text{H}_2\text{S}}$ values coincide within the $\delta^{34}\text{S}_{\text{H}_2\text{S}}$ range for magmatic fluids (i.e., -3‰ to 3‰) defined by Ohmoto and Rye (1979).

Post-mineralization-stage (stage 5) veins contain coeval anhydrite and pyrite. Assuming that sulfur isotope equilibrium was maintained between the anhydrite-pyrite mineral pairs and that the SO_4^{2-} to H_2S ratio remained constant during cooling of the low-pH (< 3) post-mineralization-stage hydrothermal fluid, the initial unfractionated sulfur isotope composition ($\delta^{34}\text{S}_{\text{SS}}$) of the fluid is calculated using regression lines for the anhydrite and pyrite $\delta^{34}\text{S}$ values (Fig. 12 ii). The convergence of the lines at $\Delta^{34}\text{S} = 0$ approximates the value for $\delta^{34}\text{S}_{\text{SS}}$, whereas the slopes of the regression line define the mole fractions of oxidized (XSO_4^{2-}) and reduced sulfur (XH_2S) in the system (Field and Gustafson 1976; Kusakabe et al. 1984). At Kames South, the stage 5 hydrothermal fluid has a calculated $\delta^{34}\text{S}_{\text{SS}}$ value of 2.2‰ , with XSO_4^{2-} and XH_2S ratios of 0.08 and 0.92, respectively. The $\delta^{34}\text{S}_{\text{SS}}$ value for the stage 5 fluid is consistent with derivation from a granitic magma

source since fluids from these melts commonly have a $\delta^{34}\text{S}_{\text{fluid}}$ value range of -3‰ to 7‰ (Ohmoto and Rye 1979).

Oxygen and carbon isotope constraints

Carbon isotope values for hydrothermal calcite are controlled by the initial fluid and wall rock isotope values, temperature, and the proportion of dissolved carbon species in the fluid (Zheng and Hoefs 1993). Methane was not observed in trapped fluid inclusions in the veins and is assumed to be negligible, with CO_2 being the dominant carbon species in the Kames South hydrothermal fluids. A temperature of 380°C , which represents average fluid trapping temperatures for stage 2 and 3 veins, was used to calculate $\delta^{13}\text{C}_{\text{CO}_2}$ values for these veins. At this temperature, the $\delta^{13}\text{C}$ fractionation between calcite and CO_2 in the hydrothermal fluid results in a $\Delta_{\text{calcite-CO}_2}$ value of -2.6‰ (Ohmoto and Rye 1979). This $\Delta_{\text{calcite-CO}_2}$ value is acceptable given that a $\pm 100^\circ\text{C}$ change in temperature equates to a minor change in the $\Delta_{\text{calcite-CO}_2}$ value of $< 0.8\text{‰}$. Hence, calculated $\delta^{13}\text{C}_{\text{CO}_2}$ values for stage 2 veins are 3.0‰ and 3.1‰ ($n = 2$), whereas calculated $\delta^{13}\text{C}_{\text{CO}_2}$ values for stage 3 veins range from -1.2‰ to 2.7‰ (mean = $0.8 \pm 1.6\text{‰}$, $n = 4$). Post-mineralization-stage calcite \pm zeolite \pm quartz \pm chlorite \pm pyrite veins most likely formed at temperatures below about 200°C . Given this temperature and the assumptions listed above, the $\delta^{13}\text{C}$ fractionation between calcite and CO_2 in the hydrothermal fluid is negligible with a $\Delta_{\text{calcite-CO}_2}$ estimate of only -0.2‰ (Ohmoto and Rye 1979). Calculated $\delta^{13}\text{C}_{\text{CO}_2}$ values for post-mineralization-stage veins range from -0.7‰ to 0.5‰ . Oxygen isotopes have a stronger temperature dependency resulting from oxygen isotope fractionations between oxygen-bearing minerals and equilibrium waters (Taylor 1979). For stage 2 and 3 veins, an average temperature of formation of about 380°C gives a $\Delta_{\text{calcite-water}}$ value of about 3.6‰ (O'Neil et al. 1969). A $\pm 100^\circ\text{C}$ variation in the temperature estimate corresponds to a minor change in the $\Delta_{\text{calcite-water}}$ value of $< 2.6\text{‰}$. Calculated $\delta^{18}\text{O}_{\text{H}_2\text{O}}$ values for stage 2 veins are 7.9‰ and 9.0‰ ($n = 2$), whereas calculated $\delta^{18}\text{O}_{\text{H}_2\text{O}}$ values for stage 3 veins range from 6.1‰ to 8.8‰ (mean = $7.2 \pm 1.3\text{‰}$, $n = 4$). A temperature estimate of 200°C for post-mineralization-stage (stage 6) veins equates to a $\Delta_{\text{calcite-water}}$ value of about 9.5‰ (O'Neil et al. 1969) and results in a calculated $\delta^{18}\text{O}_{\text{H}_2\text{O}}$ range of 2.5‰ to 5.2‰ for the vein.

Calcite from the weakly quartz-pyrite-altered Asitka Group limestone at Kames South has a $\delta^{13}\text{C}_{\text{calcite}}$ value (i.e., 0.4‰) that is comparable to recognized $\delta^{13}\text{C}_{\text{calcite}}$ values for marble and unaltered limestone (i.e., about -3‰ to 4‰ ; Sharp 2006). However, this limestone sample has a low $\delta^{18}\text{O}_{\text{calcite}}$ value (i.e., 13.1‰) with respect to the

accepted range of $\delta^{18}\text{O}_{\text{calcite}}$ values for marble and unaltered limestone (i.e., about 15‰ to 30‰; Sharp 2006). Several other Toodogone district-scale samples of calcite from Asitka Group limestone exhibit this same relatively low $\delta^{18}\text{O}_{\text{calcite}}$ signature (e.g., Kemess North, McKinley 2006). Contact-metamorphosed rocks commonly display low $\delta^{18}\text{O}_{\text{calcite}}$ values (e.g., 10‰ to 15‰; Valley 1986) compared with less altered rock. This is interpreted to be caused by the interaction of wall rock with large volumes of meteoric and/or magmatic fluids. Hence, $\delta^{18}\text{O}_{\text{calcite}}$ values for Asitka Group limestone from Kemess South and elsewhere in the district are variably affected by the interaction between limestone and meteoric fluids and/or magmatic fluids associated with intruding plutons.

Main-stage veins have calculated $\delta^{13}\text{C}_{\text{CO}_2}$ values that overlap data for post-mineralization-stage veins; however, $\delta^{18}\text{O}_{\text{H}_2\text{O}}$ values are 1‰ to 6‰ lower for the latter veins (Fig. 13). Calculated $\delta^{13}\text{C}_{\text{CO}_2}$ and $\delta^{18}\text{O}_{\text{H}_2\text{O}}$ values for early- and main-stage veins overlap the respective isotope values for the Asitka Group limestone sample when the limestone is assumed to be in equilibrium with hydrothermal fluids at 380°C. Post-mineralization-stage veins also display calculated $\delta^{13}\text{C}_{\text{CO}_2}$ and $\delta^{18}\text{O}_{\text{H}_2\text{O}}$ values that are comparable to values for limestone that is in equilibrium with a hydrothermal fluid at 200°C (Fig. 13). In summary, O and C isotope trends for the early-, main-, and post-mineralization-stage (stage 6) veins suggest that their

$\delta^{13}\text{C}_{\text{CO}_2}$ values are strongly influenced by the interaction of these fluids with altered limestone or marble country rock. It is also possible that the granodiorite assimilated Asitka Group limestone during its emplacement, resulting in a shift in $\delta^{13}\text{C}_{\text{CO}_2}$ and $\delta^{18}\text{O}_{\text{H}_2\text{O}}$ values for the ore fluids towards limestone and marble isotope values. Post-mineralization-stage veins probably formed from metamorphic and/or meteoric fluids that interacted with limestone country rock.

Discussion

Genetic model for Kemess South

Emplacement of the granodiorite and syn-magmatic Cu–Au–Mo mineralization

Southwest–NE-directed shortening occurred before the emplacement of the Maple Leaf granodiorite at 199.6 ± 0.6 Ma and resulted in NW-striking tight to isoclinal folds, an axial planar schistosity, and parallel reverse shear zones in Permian Asitka Group country rock (Fig. 14). It is unclear if the massive Takla Group basalt was also affected by the same early shortening event. Relaxation in this shortening direction coincided with the intrusion of first-generation gabbro dikes in Asitka Group rocks parallel to bedding and the existing NW-striking cleavage. Granodiorite intruded Asitka and Takla Group rocks at a depth greater than about 2 km via stoping and assimilation of these country rocks (Fig. 14 i).

Early-stage magmatic–hydrothermal ore fluids circulated via fractures through the granodiorite and proximal basalt country rock to form mineralized early-stage (stages 1 and 2) veins with enveloping potassic alteration zones. Stable isotopes for vein minerals indicate that the ore fluids were sourced mainly from the granodiorite but interacted with Asitka Group limestone country rock before metal deposition. Although propylitic alteration mineral assemblages (i.e., albite–epidote–chlorite–carbonate) were not observed in this study, they are documented by Rebagliati et al. (1995) in Takla Group basalt distal to the granodiorite. They suggest the involvement of cooler externally derived fluids in distal areas of the porphyry system (Seedorff et al. 2005; Sillitoe 2000). The main Cu–Au–Mo mineralization event is associated with stage 3 veins and coincides with the transition from potassic to phyllic or intermediate argillic alteration. Stable isotope values for the main-stage ore fluids suggest that the fluids and metals originated from the granodiorite but interacted with altered limestone and perhaps meteoric and/or metamorphic fluids in country rock near the site of metal deposition. Late-stage (stage 4) veins also display a mixed isotope signature, indicating the

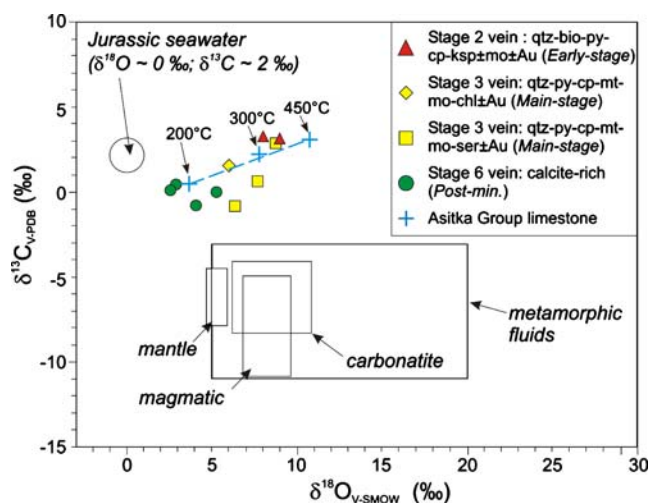
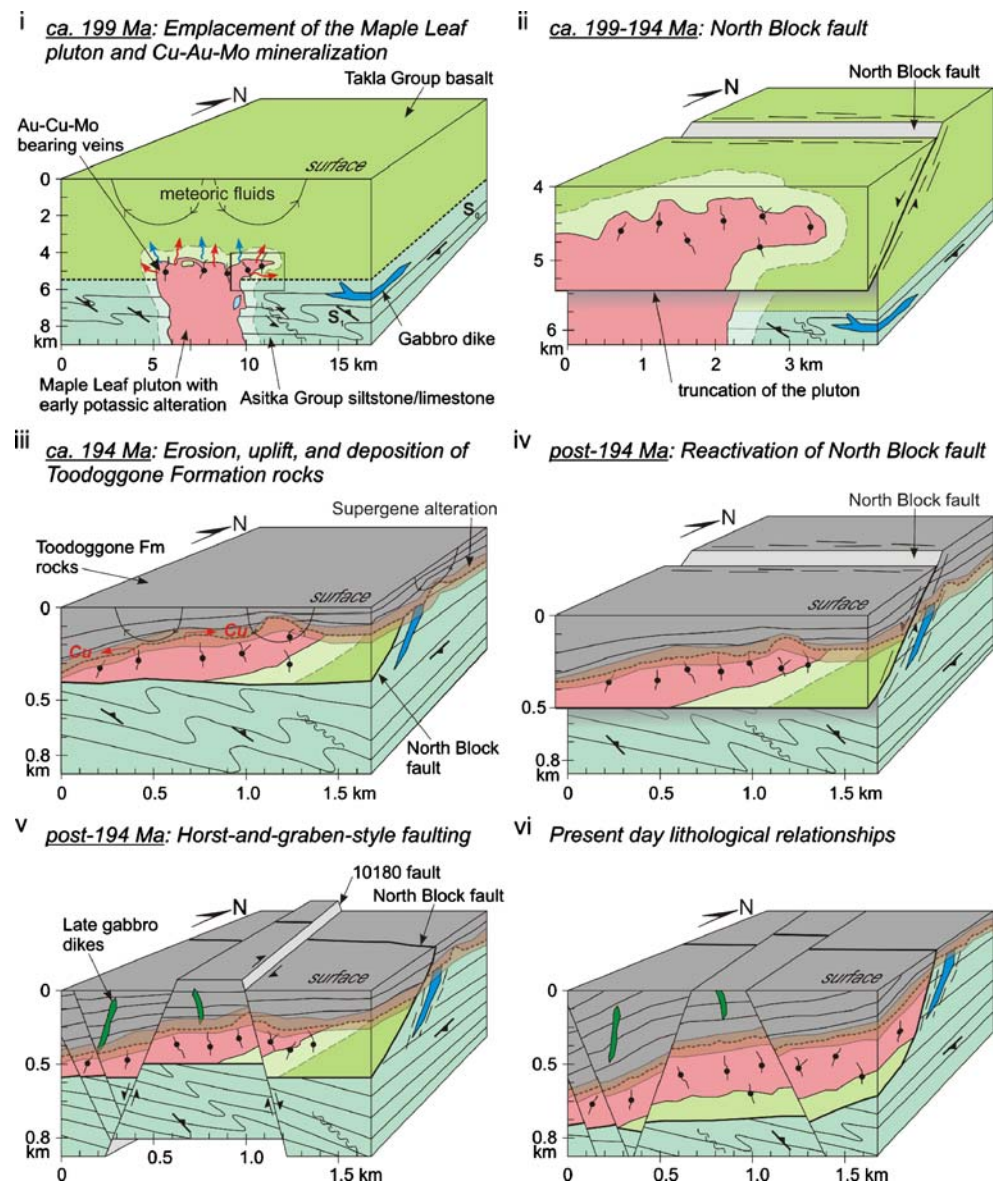


Fig. 13 Oxygen and carbon isotope fluid values are shown for early- (stage 2), main- (stage 3), and post-mineralization-stage (stage 6) veins from Kemess South. Also plotted for comparison are calculated $\delta^{18}\text{O}_{\text{H}_2\text{O}}$ and $\delta^{13}\text{C}_{\text{CO}_2}$ values for a weakly quartz–pyrite-altered Kemess South Asitka Group limestone sample that is assumed to be in equilibrium with a hydrothermal fluid at 200°C, 300°C, or 450°C. Line boxes represent data fields reported by Sharp (2006). The Jurassic seawater values are from Veizer et al. (1999). Abbreviations: *bio*, biotite; *bn*, bornite; *chl*, chlorite; *cp*, chalcopyrite; *ksp*, alkali feldspar; *mo*, molybdenite; *mt*, magnetite; *py*, pyrite; *qtz*, quartz. Abbreviations: *bio*, biotite; *chl*, chlorite; *cp*, chalcopyrite; *ksp*, alkali feldspar; *mo*, molybdenite; *mt*, magnetite; *py*, pyrite; *qtz*, quartz

Fig. 14 Genetic model for the Kemess South deposit that describes: (i) the emplacement of the Maple Leaf granodiorite into deformed Asitka Group and more massive Takla Group rocks, followed by porphyry Cu–Au–Mo mineralization; (ii) the early truncation and offset of the country rock stratigraphy and ore body by the North Block fault; (iii) the erosion, uplift, and deposition of Toodoggone Formation rocks, coinciding with supergene alteration and mineralization; (iv) the late reactivation of the North Block fault to offset Toodoggone Formation rocks; and (v) the late horst-and-graben-style dismemberment of the ore body to form (vi) present-day geological relationships



interaction between magma-derived fluids and country rock, as well as meteoric and/or metamorphic fluids. Post-mineralization-stage (stage 5) veins have anhydrite–pyrite equilibrium mineral pair sulfur isotope relationships that suggest that they formed from Cu–Au–Mo-poor hydrothermal fluids sourced from a magma, but which interacted with country rock, meteoric, and/or metamorphic fluids. The stage 6 veins probably formed from a lower-temperature (<200°C) metal-poor possibly metamorphic fluid that interacted with limestone and basalt country rock and possibly meteoric water.

Truncation of the granodiorite, ore body, and country rocks by the North Block fault

The North Block fault formed as a result of N–S-directed extension after the emplacement of the granodiorite at ca.

199 Ma but before the deposition of the Toodoggone Formation rocks at ca. 194 Ma. The fault clearly truncates the granodiorite, but it is difficult to determine to what extent it controls the present morphology of the granodiorite due to the rarity of preserved intrusive contacts between the granodiorite and country rocks. The shallow SW-plunging granodiorite at Kemess South might be a sill-like apophysis from a larger deeper pluton (Fig. 14 i), a tectonic artifact of normal faulting associated with the North Block fault, or both (Fig. 14 ii).

Erosion, uplift, and deposition of the Toodoggone Formation

Within a 5-m.y. interval, constrained by the emplacement age for the granodiorite and the depositional age for overlying Toodoggone Formation rocks, the roof of the

granodiorite pluton and surrounding country rocks were uplifted from an emplacement depth of over 2 km and exposed at the paleosurface (Fig. 14 iii). Supergene alteration of the granodiorite resulted in the widespread kaolinization of feldspars, martitization of magnetite, and hematization of ferromagnesian igneous and hydrothermal minerals. Supergene alteration in the granodiorite is divided into an upper hematite-altered leached zone that contains relatively low concentrations of Cu and a lower zone that contains less hematite but is enriched in remobilized Cu. It is probable that oxidized meteoric water at Kemess South reacted with hypogene pyrite in sericite–pyrite-altered granodiorite to form acidic water that dissolved hypogene Cu sulfide minerals above the water table and transported the Cu downwards towards the saturated zone beneath the water table. Supergene Cu sulfides precipitated by the neutralization of acidic waters, as well as by the substitution of Cu for Fe and other relatively electronegative metals in hypogene sulfide minerals by cation-exchange reactions (Sillitoe 2005). Toodoggone Formation conglomerate does not contain any hypogene sulfide minerals to react with Cu-rich groundwater; hence, argillization of feldspars in the conglomerate may have elevated the pH of the fluid, which caused the precipitation of supergene Cu oxide minerals in these rocks (Sillitoe 2005).

Copper was also remobilized from the oxidized granodiorite and reprecipitated in overlying, highly porous, and permeable Toodoggone Formation basal conglomerate beds by the circulation of oxidized meteoric fluids that flowed along the low-permeability barrier created by the granodiorite nonconformable contact. Repeated vertical fluctuations in the level of the water table and the lateral migration of the water along the low-permeability granodiorite contact most likely encouraged the dissolution, redistribution, and reprecipitation of Cu in granodiorite and Toodoggone Formation units either side of the contact. The greater enrichment of Cu relative to Au in the lower portions of the supergene-altered granodiorite (Fig. 9 ii) suggests that Cu has commonly been remobilized by meteoric fluids, whereas Au has been relatively resistant to chemical remobilization. Hypogene gold is only locally mechanically eroded, reworked, and deposited as detrital grains in paleotopographic depressions along the Toodoggone Formation basal contact.

Reactivation of the North Block fault and horst-and-graben-style dismemberment of the ore body

A resumption in regional N–S-directed extension after the deposition of the Toodoggone Formation led to the reactivation of the North Block fault and the normal displacement of these rocks (Fig. 14 iv). The transition to E–W-directed extension resulted in the formation of

dextral–normal NW-trending faults (e.g., the 10180 fault) and co-temporal NE-trending normal faults. The NW- to NE-trending faults resulted in the horst-and-graben block faulting of the mine stratigraphy and ore body (Fig. 14 v). Late NE-striking gabbro dikes intruded along NE-striking fractures in Toodoggone Formation units during NE–SW-directed shortening (Fig. 14 vi).

Conclusions

Copper–Au–Mo mineralization at Kemess South is mainly hosted by the tabular, moderately SW-plunging, 199.6 ± 0.6 -Ma Maple Leaf granodiorite. The pluton intrudes folded, mostly SW-dipping (35° to 65°), Permian Asitka Group siltstone and limestone and Triassic Takla Group basalt. These units are unconformably overlain by 194.0 ± 0.4 -Ma Toodoggone Formation conglomerate, volcanoclastic, and epiclastic rocks. The granodiorite displays an intrusive contact with Takla Group basalt but a sheared contact with Asitka Group rocks. Although Cu–Au–Mo mineralization is mainly hosted by the granodiorite, minor ore zones are also hosted by basalt within 50 m of the intrusive contact. Low-tonnage high-grade Cu zones occur beneath a 30-m-thick leached capping in supergene-altered granodiorite and in exotic positions in overlying Toodoggone Formation rocks.

Both granodiorite and basalt possess comparable vein paragenesis and alteration histories, with minor variations in hydrothermal mineral assemblages caused by differing protolith chemistry. Early potassic alteration (and early-stage Cu \pm Au \pm Mo mineralization) is commonly replaced by phyllic and intermediate argillic alteration related to the main-stage Cu–Au–Mo mineralization event. Late-stage pyrite-rich stringer veins are cut by post-mineralization-stage anhydrite-rich, carbonate-rich, and chlorite veins. The North Block fault is an E-striking steeply S-dipping normal fault or shear zone that juxtaposes the granodiorite/basalt-hosted ore body and unmineralized Asitka Group rocks. Movement on the fault probably took place during at least two deformation events, occurring before and after the deposition of the Toodoggone Formation rocks. Younger NW- and NE-striking normal–dextral faults cut all rock types, orebodies, and the North Block fault, with displacements of <100 m, and result in the graben-and-horst-style block faulting of the stratigraphy and ore body.

Acknowledgments The Kemess South study is part of a larger NSERC-CRD grant research project between the University of British Columbia, Northgate Minerals Ltd., and Stealth Minerals Ltd. The latter two companies are thanked for providing generous financial and logistical support for fieldwork in the Toodoggone district. Carl Edmunds, Brian Kay, Ron Konst, Brian O'Connor, Gary Parrup, and

Chris Rockingham from Northgate Minerals Ltd. are thanked for providing logistical support and access to the Kerness South pit and drill core. Field assistants, Andy Orr and Colin Smith, contributed greatly with their enthusiasm and dedication during fieldwork and subsequent laboratory work. Greg Dipple is thanked for his advice regarding the interpretation of C and O isotope data. Greg Arehart, Thomas Bissig, Alan H. Clark, Jean Cline, Steve Garwin, Steve Kesler, David Love, W.J. McMillan, and Larry Meinert are thanked for their careful reviews of the manuscript and helpful comments. The first author acknowledges financial support from the second stage of the Brain Korea 21 project at Pukyong National University. The Radiogenic Isotope Facility at the University of Alberta is supported, in part, by an NSERC Major Resources Support Grant.

References

- Al-Asam IS, Taylor BE, South B (1990) Stable isotope analysis of multiple carbonate samples using selective acid extraction. *Chem Geol Isot Geosci* 80:119–125
- Bodnar RJ (1994) Synthetic fluid inclusions. XII: The system H₂O–NaCl. Experimental determination of the halite liquidus and isochores for a 40 wt.% NaCl solution. *Geochim Cosmochim Acta* 58:1053–1063
- Bodnar RJ, Vityk MO (1994) Interpretation of microthermometric data for NaCl–H₂O fluid inclusions. In: De Vivo B, Frezzotti ML (eds) *Fluid inclusions in minerals: methods and applications*. Virginia Polytechnic Institute and State University, Blacksburg, pp 117–131
- Bodnar RJ, Burnham CW, Sterner SM (1985) Synthetic fluid inclusions in natural quartz. III: determination of phase equilibrium properties in the system H₂O–NaCl to 1000 degrees C and 1500 bars. *Geochim Cosmochim Acta* 49:1861–1873
- Brown PE, Hagemann SG (1995) MacFlinCor and its application to fluids in archaean lode-gold deposits. *Geochim Cosmochim Acta* 59:3943–3952
- Clark JR, Williams-Jones AE (1991) 40Ar/39Ar ages of epithermal alteration and volcanic rocks in the Toodoggone Au–Ag district, north-central British Columbia (94E). British Columbia Ministry Energy, Mines and Petroleum Research, Geological Fieldwork 1990, Paper 1991-1, pp 207–216
- Claypool GE, Holser WT, Kaplan IR, Sakai H, Zak I (1980) The age curves of sulfur and oxygen isotopes in marine sulfate and their mutual interpretation. *Chem Geol* 28:199–260
- Coplen TB, Kendall C, Hopple J (1983) Comparison of stable isotope reference samples. *Nature* 302:236–238
- Diakow LJ (2001) Geology of the southern Toodoggone River and northern McConnell Creek map areas, north-central British Columbia. British Columbia Ministry of Energy, Mines and Petroleum Resources, Open file map 2001-1, 1:50,000 scale
- Diakow LJ (2004) Geology of the Samuel Black Range between the Finlay river and Toodoggone river, Toodoggone river map area, north-central British Columbia (parts of NTS 94E/2, 6 and 7). British Columbia Ministry of Energy, Mines and Petroleum Resources, Open file map 2004-4, 1:50,000 scale
- Diakow LJ (2006a) Geology between the Finlay River and Chukachida Lake, central Toodoggone River map area, north-central British Columbia (parts of NTS 94E/2, 6, 7, 10 and 11). British Columbia Ministry of Energy, Mines and Petroleum Resources, Open file map 2006-4, 1:50,000 scale
- Diakow LJ (2006b) Toodoggone's Au–Cu setting unraveled. *Mineral Exploration Roundup* 06. Westin Bayshore, Vancouver, pp 14–15
- Diakow LJ, Panteleyev A, Schroeter TG (1991) Jurassic epithermal prospects in the Toodoggone river area, northern British Columbia: examples of well preserved, volcanic-hosted, precious metal mineralization. *Econ Geol* 86:529–554
- Diakow LJ, Panteleyev A, Schroeter TG (1993) Geology of the Early Jurassic Toodoggone Formation and gold-silver deposits in the Toodoggone river map area, northern British Columbia. British Columbia Ministry of Energy, Mines and Petroleum Resources, pp 72
- Diakow LJ, Nixon GT, Rhodes R, Lane B (2005) Geology between the Finlay and Toodoggone rivers, Toodoggone river map area, north-central British Columbia (parts of NTS 94E/2, 6 and 7). British Columbia Ministry of Energy, Mines and Petroleum Resources, Open file map 2005-3, 1:50,000 scale
- Dickinson JM (2006) Jura–Triassic magmatism and porphyry Au–Cu mineralization at the Pine deposit, Toodoggone district, north-central British Columbia. M.Sc. thesis, University of British Columbia, Vancouver, pp 116
- Duuring P, Rowins SM, Dickinson JM, McKinley BSM, Diakow LJ, Kim Y-S, Creaser RA (2008) Examining potential genetic links between Jurassic porphyry Cu–Au ± Mo and epithermal Au ± Ag mineralization in the Toodoggone district of north-central British Columbia, Canada. *Miner Deposita* (this volume)
- Field CW, Gustafson LB (1976) Sulfur isotopes in the porphyry copper deposit at El Salvador, Chile. *Econ Geol* 71:1533–1548
- Goldstein RH, Reynolds TJ (1994) Systematics of fluid inclusions in diagenetic minerals. *SEPM Short Course* 31:199
- Hagemann SG, Brown PE (1996) Geobarometry in archaean lode-gold deposits. *Eur J Mineral* 8:937–960
- Kusakabe M, Nakagawa S, Hori M, Matsuhisa Y, Ojeda JM, Serrano L (1984) Oxygen and sulfur isotopic compositions of quartz, anhydrite and sulfide minerals from the El Teniente and Rio Blanco porphyry copper deposits, Chile. *Bull Geol Surv Jpn* 35:583–614
- Macdonald AJ, Spooner ETC (1981) Calibration of a Linkam TH 600 programmable heating–cooling stage for microthermometric examination of fluid inclusions. *Econ Geol* 76:1248–1258
- Markey RJ, Stein HJ, Morgan JW (1998) Highly precise Re–Os dating for molybdenite using alkaline fusion and NTIMS. *Talanta* 45:935–946
- Markey RJ, Stein HJ, Hannah JL, Selby D, Creaser RA (2007) Standardizing Re–Os geochronology: a new molybdenite reference material (Henderson, USA) and the stoichiometry of Os salts. *Chem Geol* 244:74–87
- McKinley BSM (2006) Geological characteristics and genesis of the Kerness North porphyry Au–Cu–Mo deposit, Toodoggone district, north-central British Columbia, Canada. M.Sc. thesis, University of British Columbia, Vancouver, British Columbia, Canada, pp 136
- Monger J, Church B (1977) Revised stratigraphy of the Takla Group, north-central British Columbia. *Can J Earth Sci* 14:318–326
- Monger JWH, Nokleberg WJ (1996) Evolution of the northern North American Cordillera: generation, fragmentation, displacement, and accretion of successive North American plate margin arcs. *Geology and Ore Deposits of the American Cordillera, Reno/Sparks*, pp 1133–1152
- Mortensen JK, Ghosh DK, Ferri F (1995) U–Pb geochronology of intrusive rocks associated with copper–gold porphyry deposits in the Canadian Cordillera. In: Schroeter TG (ed) *Porphyry deposits of the northwestern Cordillera of North America*. Canadian Institute of Mining and Metallurgy, Montreal, pp 142–160
- Ohmoto H, Lasaga AC (1982) Kinetics of reactions between aqueous sulfates and sulfides in hydrothermal systems. *Geochim Cosmochim Acta* 46:1727–1745
- Ohmoto H, Rye RO (1979) Isotopes of sulfur and carbon. In: Barnes HL (ed) *Geochemistry of hydrothermal ore deposits*. 2nd edn. Wiley, New York, pp 509–567

- O'Neil JR, Clayton RN, Mayeda TK (1969) Oxygen isotope fractionation in divalent metal carbonates. *J Chem Phys* 51:5547–5558
- Rebagliati CM, Bowen BK, Copeland DJ, Niosi DWA (1995) Kames South and Kames North porphyry gold-copper deposits, northern British Columbia. In: Schroeter TG (ed) *Porphyry deposits of the northwestern Cordillera of North America*. Canadian Institute of Mining and Metallurgy, Montreal, pp 377–396
- Roedder E (1984) Fluid inclusions. *Rev Mineral* 12:644
- Roedder E, Bodnar RJ (1980) Geologic pressure determinations from fluid inclusion studies. *Annu Rev Earth Planet Sci* 8:263–301
- Rollinson HR (1993) Using geochemical data: evaluation, presentation, interpretation. Longman, Harlow, p 352
- Seedorff E, Dilles JH, Proffett JM Jr., Einaudi MT, Zurcher L, Stavast WJA, Johnson DA, Barton MD (2005) Porphyry deposits; characteristics and origin of hypogene features. *Econ Geol* 100th Anniversary Volume:251–298
- Selby D, Creaser RA (2004) Macroscale NTIMS and microscale LA-MC-ICP-MS Re–Os isotopic analysis of molybdenite; testing spatial restrictions for reliable Re–Os age determinations, and implications for the decoupling of Re and Os within molybdenite. *Geochim Cosmochim Acta* 68:3897–3908
- Sharp Z (2006) *Principles of stable isotope geochemistry*. Pearson Prentice Hall, Upper Saddle River, p 344
- Shepherd TJ, Rankin AH, Alderton DHM (1985) *A practical guide to fluid inclusion studies*. Blackie, Glasgow, p 239
- Sillitoe RH (2000) Gold-rich porphyry deposits; descriptive and genetic models and their role in exploration and discovery. *Rev Econ Geol* 13:315–345
- Sillitoe RH (2005) Supergene oxidized and enriched porphyry copper and related deposits. *Econ Geol* 100th Anniversary Volume:723–768
- Taylor HP Jr. (1979) Oxygen and hydrogen isotope relationships in hydrothermal mineral deposits; 2. In: Barnes HL (ed) *Geochemistry of hydrothermal ore deposits*. Wiley, New York, pp 236–277
- Turner FJ (1981) *Metamorphic petrology: mineralogical, field, and tectonic aspects*. McGraw-Hill, New York, p 524
- Valley JW (1986) Stable isotope geochemistry of metamorphic rocks. *Rev Mineral* 16:445–489
- Veizer J, Ala D, Azmy K, Bruckschen P, Buhl D, Bruhn F, Carden GAF, Diener A, Ebner S, Godderis Y, Jasper T, Korte C, Pawellek F, Podlaha OG, Strauss H (1999) $^{87}\text{Sr}/^{86}\text{Sr}$, $\delta^{13}\text{C}$ and $\delta^{18}\text{O}$ evolution of Phanerozoic seawater. *Chem Geol* 161:59–88
- Zheng YF, Hoefs J (1993) Carbon and oxygen isotopic covariations in hydrothermal calcites; theoretical modeling on mixing processes and application to Pb–Zn deposits in the Harz Mountains, Germany. *Miner Deposita* 28:79–89